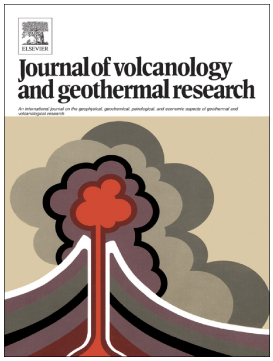

Morphological and multivariate statistical analysis of quaternary monogenetic vents in the Central Anatolian Volcanic Province (Turkey): Implications for the volcano-tectonic evolution

Göksu Uslular, Nicolas Le Corvec, Francesco Mazzarini, Denis Legrand, Gonca Gençalioğlu-Kuşcu

PII: S0377-0273(21)00109-8

DOI: https://doi.org/10.1016/j.jvolgeores.2021.107280

Reference: VOLGEO 107280

To appear in: *Journal of Volcanology and Geothermal Research*

Received date: 5 December 2020

Revised date: 10 May 2021

Accepted date: 12 May 2021

Please cite this article as: G. Uslular, N. Le Corvec, F. Mazzarini, et al., Morphological and multivariate statistical analysis of quaternary monogenetic vents in the Central Anatolian Volcanic Province (Turkey): Implications for the volcano-tectonic evolution, *Journal of Volcanology and Geothermal Research* (2021), https://doi.org/10.1016/j.jvolgeores.2021.107280

Morphological and Multivariate Statistical Analysis of Quaternary Monogenetic Vents in the Central Anatolian Volcanic Province (Turkey): Implications for the Volcano-Tectonic Evolution

Göksu Uslular [a,b]*, Nicolas Le Corvec [c], Francesco Mazzarini [d], Denis Legrand [e], Gonca Gençalioğlu-Kuşcu [a]

[a] Department of Geological Engineering, Muğla Sıtkı Koçman University, Kötekli Campus, 48000 Muğla, Turkey

[b] Department of Earth Sciences, University of Geneva, Rue des Maraîchers 13, 1205 Geneva, Switzerland

[c] Independent Researcher, 33200 Bordeaux, France

[d] Istituto Nazionale di Geofisica e Vulcanologia (INGV), Via Cesare Battisti, 53, 56125 PISA Italy

[e] Universidad Nacional Autonoma de Mexico (UNAM), Mexico City, Mexico

*Corresponding author: goksuuslular@mu.edu.tr; goeksu.uslular@etu.unige.ch

ABSTRACT

The interaction and competition between magmatic and tectonic processes mostly control the spatial distribution and morphology of monogenetic volcanoes. The Central Anatolian Volcanic Province, situated in a strike-slip environment, provides a remarkable opportunity to understand this relationship. We defined six monogenetic clusters and analyzed 540 Quaternary monogenetic volcanoes in terms of morphological and spatial characteristics. There is no distinct correlation among the morphological parameters of scoria cones or lava domes, possibly owing to the various factors and the sporadic nature of magmatic activity in the region. Our detailed multivariate statistical and vent alignment analyses together with several implications in the literature reveal that the CAVP is a tectonically-controlled intraplate volcanic field, which is mostly driven by regional deformations. The presence of both

clustered and non-clustered vent distributions and the petrological characteristics of the volcanics within the region indicates that the dikes are derived directly by the pre-existing melt-bearing heterogeneous mantle (i.e., Eğrikuyu monogenetic field) or the independent and short-lived shallow or deep crustal magma reservoirs (i.e., Nevşehir-Acıgöl volcanic field). The local changes in the stress regimes and crustal lithology result in variations of field shape, spatial vent distribution, and vent alignments throughout the region. The triggering mechanisms for the initiation of the Quaternary volcanism in the region can be the lithospheric-scale Central Anatolian fault zone, here considered as an immature rift zone where Erciyes volcanic field is developed and behaves as a possible magmatic transfer zone. Tuz Gölü fault zone as a western border of the so-called rift basin in the region is mostly responsible for the crustal propagation of magma, and the kinematic changes along this fault zone (i.e., strike-slip to normal) mostly shaped the spatial vent distributions and alignments of the clusters in its close proximity (e.g., Hasandağ-Keçiboyduran volcanic field).

Keywords: Self-similar clustering, Vent alignment, Strike-slip tectonism, Monogenetic volcanism, Central Anatolian Volcanic Province

1. Introduction

Monogenetic volcanic fields host the most common volcanic landforms on Earth and can be found in all tectonic settings. Monogenetic edifices are small volume volcanoes (< 1 km^3) formed by a single eruptive episode which may have a duration from days to decades and include many different eruptive styles driven by the expansion of magmatic volatiles with or without the involvement of ground- or surface water (phreatomagmatic) (Valentine and Connor, 2015). The surface morphology of these volcanoes is affected by internal (e.g., magma rheology, rate of ascent, and magma/water ratio) and external (e.g., tectonic features, climate) factors to produce various types, including scoria cones, maars (maar-diatremes), spatter cones, lava domes, tuff cones and tuff rings (e.g., Valentine et al., 2005; 2007; White and Ross, 2011; Németh, 2010; Pedrazzi et al., 2013; Németh and Kósik, 2020). Scoria cones and maars, which are generally mafic to intermediate in composition, are the most common monogenetic edifices (Lorenz, 1975; Settle, 1979; Wood, 1980a; Lorenz, 2007; Graettinger, 2018). One to several hundreds of volcanic centers (or vents) can either be found in the isolated volcanic fields (e.g., Michoacan-Guanajuato Volcanic Field, Mexico; Connor, 1987) or at the flanks of polygenetic volcanoes (e.g., Mauna Kea Volcano, Porter, 1972; Mount Etna Volcano, Mazzarini and Armienti, 2001). The spatial distribution of vents has been analyzed by different methods for several decades to understand the link

between tectonism and magmatism (e.g., Connor, 1987; White and Ross, 2011; Le Corvec et al., 2013a; Muirhead et al., 2015; Valentine and Connor, 2015; Haag et al., 2019; Murcia et al., 2019; Cañón-Tapia, 2020). As each vent represents the last point of a magma pathway en-route to the surface either from shallow (upper crust) or deep (lower crust or mantle) magma reservoirs, their alignment and/or clustering represent the possible surface expressions of the underlying magma plumbing systems, especially in the brittle upper crust (e.g., Brenna et al., 2011; Germa et al., 2013; Le Corvec et al., 2013a; Muirhead et al., 2015).

The morphological analysis of monogenetic volcanoes (mostly scoria cones) also provides new insights into the understanding of both internal and external factors in their formation (e.g., Wood, 1980a; Hooper and Sheridan, 1998; Riedel et al., 2003; Dóniz et al., 2008; Favalli et al., 2009; Rodriguez-Gonzalez et al., 2010; Inbar et al., 2011; Kereszturi et al., 2012; Kervyn et al., 2012; Bemis and Ferencz, 2017). The morphometry-based studies mostly tackled the reasons for various sizes and shape, and the factors (e.g., magma rheology, original eruptive facies, degradation processes, climate) responsible for these morphometric differences in monogenetic volcanoes (Wood, 1980b; Hooper and Sheridan, 1998; Valentine et al., 2007). Most of the interpretations related to morphology have been generally considered as indirectly contributing to the tectonomagmatic evolution of volcanic fields, but the role of fault geometry in the eruptive dynamics and morphology has only been recently revealed (Gómez-Vasconcelos et al., 2020). There are also many attempts to explore the possible link between the age and the morphology of scoria cones (i.e., relative chronology), and also a few more suggesting the fractal behavior of size-distribution (i.e., width of scoria cones, Kurokawal et al., 1995; Pérez-López et al., 2011; Uslular et al., 2015).

We performed morphological, statistical (self-similar clustering, principal component, vent-to-vent distance, Poisson nearest neighbor), and vent alignment analyses on Quaternary monogenetic vents in the Central Anatolian Volcanic Province (CAVP), one of the most spectacular volcanic fields in Anatolia with various types of Miocene-Quaternary polygenetic and several hundreds of Quaternary monogenetic volcanoes (Toprak, 1998) (Figs. 1A and B). We defined six volcanic clusters (Fig. 1B) by slightly modifying the previous clustering (Toprak, 1998) and considering the volcanological evolution of the regions revealed by well-established literature. We also revised the comprehensive vent database of Arcasoy (2001) by selecting the Quaternary monogenetic vents (540) and classified them based on their types (i.e., scoria cone, lava dome, and maar). We focused especially on the scoria cones and lava domes to define their morphological characteristics and to create a link between their spatial distributions and

the tectonism in the CAVP. Our approach presented in this study contributes new understanding of the role of tectonism on the widespread volcanism in the region (e.g., Pasquare et al., 1988; Göncüoğlu and Toprak, 1992; Toprak and Göncüoglu, 1993; Dhont et al., 1998; Toprak, 1998) by providing new insight into the mechanical behavior of the crust beneath the region.

2. Quaternary Monogenetic Clusters in the CAVP

Central Anatolia is a high plateau (~ 1 km a.s.l; Çiner et al., 2015) located at the Kırşehir block between Pontide and Anatolide-Tauride orogenic mountain belts (e.g., Okay and Tüysüz, 1999) (Fig. 1A). Volcanism initiated in the late Cretaceous within the Sakarya zone (NW of Kırşehir block; Galatia volcanics; *ca.* 76 Ma, Koçyiğit and Beyhan, 1998) during the almost coeval closure of the northern Neo-Tethys ocean along the İzmir-Ankara-Erzincan suture zone (e.g., Okay and Tüysüz, 1999; Pourteau et al., 2013) (Fig. 1A). After the initiation of a collision between Arabian and Eurasian plates along the Bitlis suture zone that resulted in the closure of the southern Neo-Tethys during the middle Miocene (Okay et al., 2010; Cavazza et al., 2018), the volcanism continued in the Galatia (*ca.* 19 Ma to Pliocene?; Wilson et al., 1997) and spread throughout the approximate borders of Kırşehir block (Karacadağ to the west, *ca.* 21-14 Ma, Asan and Kurt, 2011; Erenlerdağ-Alacadağ-Sulutaş to the southwest, *ca.* 22-3 Ma, e.g., Gençoğlu-Korkmaz et al., 2017; Sivas to the east, *ca.* 23-4 Ma, e.g., Kocaarslan and Ersoy, 2018; Reid et al., 2019). The CAVP within this region is located at the southern part of Kırşehir block and extends through the Anatolide-Tauride platform as a NE-SW trending volcanic belt bounded by two major transcurrent fault zones, namely the Tuz Gölü (hereafter western border fault) and Central Anatolian (hereafter eastern border fault) with its southern component the Ecemiş fault (Toprak and Göncüoglu, 1993; Koçyiğit and Beyhan, 1998; Çemen et al., 1999; Koçyiğit and Erol, 2001) (Fig. 1B). The preceding NNW-SSE to NE-SW compressional stress regime tailed off in the late Miocene (e.g., Özsayın et al., 2013), and subsequently, the N-S to NE-SW trending extensional regime became active (Göncüoğlu and Toprak, 1992; Dhont et al., 1998). The timing of widespread volcanism, which initiated during the middle Miocene and continued to the Holocene, has been constrained by geochronology data (13.7 ± 0.3 Ma, K-Ar, Keçikalesi caldera, Besang et al., 1977; 8.97 ± 0.64 ka, (U-Th)/He, 2σ, Hasandağ stratovolcano, Schmitt et al., 2014; Fig. 1B).

There are some recent attempts to explore this relatively complex geodynamic setting and its role in the evolution of widespread CAVP volcanism (Bartol and Govers, 2014; Delph et al., 2017; Göğüş et al.,

2017; Reid et al., 2017; Di Giuseppe et al., 2018; Rabayrol et al., 2019). Roll-back of the Cyprus slab since early or middle Miocene resulted in the delamination or dripping of the sub-continental lithospheric mantle (Biryol et al., 2011; Bartol and Govers, 2014; Abgarmi et al., 2017; Delph et al., 2017; Göğüş et al., 2017; Rabayrol et al., 2019). This has been interpreted to have caused asthenospheric upwelling, which resulted in related mantle melting (e.g., Delph et al., 2017) and the initiation of the CAVP volcanism (especially ignimbrite flare-ups; e.g., Aydar et al., 2012). Subsequent break-off of the subducting African lithosphere, which is coeval with the uplift of central Anatolia (*ca.* 8 Ma; Cosentino et al., 2012; Schildgen et al., 2014), lead to the upwelling of asthenosphere that has been linked with the late Miocene to recent volcanism in the CAVP (Abgarmi et al., 2017; Delph et al., 2017; Reid et al., 2017; Schleiffarth et al., 2018). In summary, the CAVP developed within an extensional tectonic regime and above a *ca.* 35-40 km thick crust exhibiting low seismic velocity layers ranging from 15 to 25 km depth (possible crustal magma reservoirs; Abgarmi et al., 2017) that overlies a relatively thin metasomatized lithospheric mantle and an underlying hot asthenosphere.

The CAVP exhibits many spectacular volcanic landscapes including Miocene-Pliocene widespread ignimbrites (e.g., Aydar et al., 2012), various types of Miocene-Quaternary polygenetic volcanoes (e.g., Hasandağ and Erciyes stratovolcanoes, Keçikalesi and Acıgöl calderas) and hundreds of Quaternary monogenetic volcanoes (Toprak, 1998; Arcasoy, 2001; Arcasoy et al., 2004). These are typically in the form of scoria cones with smaller numbers of lava domes, maars, and tuff rings. Monogenetic volcanoes in the CAVP documented in this study are formed either on the flanks of polygenetic volcanoes (e.g., Erciyes stratovolcano) or as resurgent phases in calderas (e.g., Acıgöl and Derinkuyu calderas), or in the isolated volcanic fields (Eğrikuyu and Karapınar monogenetic fields) (Toprak, 1998) (Fig. 1B). They are clustered in six distinct regions (Fig. 1B) based on the spatial distributions of vents and also the volcanological evolution of the adjacent field (slightly modified after Toprak, 1998). These regions are the Erciyes, Nevşehir-Acıgöl, Derinkuyu, and Hasandağ-Keçiboyduran volcanic fields, and Eğrikuyu and Karapınar monogenetic fields (hereafter clusters 1 to 6, respectively; Fig. 1B).

The Quaternary volcanism in cluster-1 is mostly represented by the Erciyes stratovolcano stage consisting of two eruptive cycles that form numerous scoria cones and lava domes with a maar (Şen, 1997; Şen et al., 2003; Gençalioğlu-Kuşcu et al., 2007). Although a significant number of monogenetic volcanoes erupted during the Pleistocene, there are also Holocene felsic lava domes in the region (Table 1; Sarıkaya et al., 2019; Friedrichs et al., 2021). The spatial vent distribution on the flanks of Erciyes stratovolcano is almost radial (Toprak, 1998), but the main trend of vent alignment (especially those in

the southwestern flank) is N32°E based on the spatial analysis, indicating a WNW-ESE extension along the NNE trending Dündarlı-Erciyes fault (Higgins et al., 2015) (Fig. 1B).

Acıgöl (or Kocadağ) caldera located at the western part of the region (Yıldırım and Özgür, 1981) is characterized by the youngest ignimbrite deposits in the CAVP and various Quaternary monogenetic volcanoes (Druitt et al., 1995; Froger et al., 1998; Mouralis et al., 2002; Schmitt et al., 2011; Atıcı et al., 2019). The lava domes with dacitic to rhyolitic composition (e.g., Batum, 1978; Türkecan et al., 2004; Siebel et al., 2011) are the most abundant monogenetic edifices in the region (cluster-2; Table 1), and they form two temporally distinct clusters (i.e., late Pleistocene to Holocene, Schmitt et al., 2011). Maars, tuff rings, and explosion craters are the second common monogenetic volcanoes in the region (Table 1). They are mostly rhyolitic in composition, except for the basaltic trachyandesitic İcik maar and Karataş tuff ring (Türkecan et al., 2004; Aydar et al., 2011; Uslular and Gençalioğlu-Kuşcu, 2020). Scoria cones of basaltic to andesitic compositions are more dispersed within this cluster, and their formation is mostly coeval with the other monogenetic edifices based on the available geochronology data (Türkecan et al., 2004). Alignment directions are variable in this cluster (NW-SE, N-S, and NE-SW; Batum, 1978; Toprak, 1998).

The lava dome complexes, numerous scoria cones, and a maar volcano represent the Quaternary volcanism in cluster-3 (Table 1) where there is a buried caldera complex (i.e., Derinkuyu, Froger et al., 1998). Two temporarily successive buried calderas that produced widespread ignimbrites in the region also host the Quaternary dome complexes in the region (namely, Şahinkalesi and Göllüdağ; Türkecan et al., 2004; Aydin et al., 2014). The mafic scoria cones (Batum, 1978; Türkecan et al., 2004; Aydin et al., 2014) are mainly concentrated in the northern parts between lava dome complexes to the south and the Erdaş stratovolcano to the north (Fig. 2). The available geochronology data on scoria cones (Türkecan et al., 2004; Aydın et al., 2014) proclaim that their formations are mostly coeval with the lava domes. Narlıgöl is a mafic maar in the region with well-exposed pyroclastic deposits (Gevrek and Kazancı, 2000; Uslular and Gençalioğlu-Kuşcu, 2020). The vent alignment is almost identical to cluster-2 with various directions (Toprak, 1998).

The cluster-4 consists of two stratovolcanoes (namely Hasandağ and Keçiboyduran) and related numerous monogenetic volcanoes (mainly scoria cones with subordinate lava domes) (Figs. 1B and 2). The dextral western border fault zone in the CAVP and its components have a direct role in the formation of volcanism around this cluster (e.g., Toprak and Göncüoglu, 1993; Dhont et al., 1998; Toprak, 1998). The alignment of monogenetic vents in the region with a dominant trend of NW-SE also

clearly supports this claim (Toprak, 1998; Ulusoy et al., 2020). The Quaternary products of Hasandağ stratovolcano that include scoria cones, lava domes, and two maars are mostly located either at the summit or the northwestern parts of the volcano (i.e., Karataş basaltic field; Ercan et al., 1992; Aydar and Gourgaud, 1998). Keçiboyduran volcano is an early Pliocene-Quaternary stratovolcano (Aydin et al., 2014) located at the eastern part of Hasandağ stratovolcano (Fig. 2). The basaltic scoria cones and rhyolitic lava domes with related lava flows mostly represent the Quaternary phase of the stratovolcano (Aydin et al., 2014) (Fig. 2). Some of these vents are aligned with the NW-SE trending Keçiboyduran fault (Toprak and Göncüoglu, 1993).

Clusters 5 and 6 are the partly isolated monogenetic fields (Figs. 1B and 2). The clustering of monogenetic vents in cluster-5 follows two dominant trends, which are generally NE-SW in the west and mostly N-S to NW-SE toward to east (Toprak, 1998) (Figs. 1B and 2). Many aligned scoria cones in the region are the possible indications of buried faults (i.e., covered mostly by younger sediments and ignimbrite flows; Toprak, 1998; Uslular et al., 2015). There are a few basaltic maars in the region (Uslular et al., 2015; Uslular and Gençalioğlu-Kuşcu, 2020), and there is no clear temporal relationship with the formation of scoria cones based on the available age data (Ercan et al., 1992; Notsu et al., 1995; Reid et al., 2017; Doğan-Külahçı et al., 2018). The cluster-6 formed on lacustrine deposits (e.g., Kuzucuoğlu et al., 1999) and mainly consists of basaltic scoria cones, maars, and extensive lava fields (Keller, 1974) (Figs. 1B and 2). There is a good alignment of maars and adjacent scoria cones along with the NE-SW trend, which is almost parallel to the Ecemiş fault (Figs. 1B and 2). The available geochronology data reveal that the volcanism in the region has existed in the middle Pleistocene (Reid et al., 2017).

3. Methods

3.1. Morphological Measurements

The Plio-Quaternary vent database in the CAVP (Toprak, 1998; Arcasoy, 2001; Arcasoy et al., 2004) was revised by selecting the exact monogenetic edifices (n= 540) and then filtered based on their types (i.e., scoria cone, lava dome, maar, tuff ring, and undifferentiated) (Table 1). The available studies in the literature, 1:25000 scale topographic maps, different satellite and Google Earth images, and fieldwork campaigns further helped us to decipher, when possible, the type of vents. Additionally, all the available data in the literature (e.g., geochemistry, geochronology) related to each monogenetic edifice were compiled (Supplementary Material Data-S1). Maars are almost 20 in total and their morphological characteristics have been studied in detail using high-resolution drone-based digital surface models and

orthomosaics (Uslular and Gençalioğlu-Kuşcu, 2020). Therefore, we here only focus on the scoria cones and lava domes.

Morphometric measurements were performed on the scoria cones (174 out of 238) and lava domes (91 out of 166) using the Advanced Land Observing Satellite World 3D (AW3D) digital elevation models, which are the best freely available ones for the CAVP with a 30 m spatial resolution (5 m height accuracy; Tadono et al., 2015). The edifices with a height of $\leq$ 15 m were not selected for morphometric analyses as they are too small for the detection limits of 30 m resolution digital elevation models. In addition, if there is a large breaching or no clear distinction from surroundings via abrupt slope change, such cones/domes were not evaluated for morphometric analysis. The measurements were performed in four directions along with the monogenetic edifices (i.e., N-S, E-W, NE-SW, and NW-SE), and the minimum, maximum, median and mean values were calculated for each volcano (Supplementary Material Data-S1). The mean values of basic morphometric parameters (width, height, slope, and volume), which were calculated from the mean values of each volcano with 2σ standard errors, are provided in Tables 2 and 3 for each monogenetic cluster. Also, we classified the morphological types of scoria cones (Dóniz-Páez, 2015; Bemis and Ferencz, 2017) and lava domes (Blake, 1990; Fink and Griffiths, 1998; Aguirre-Díaz et al., 2006; Karatson et al., 2013) (Supplementary Material Data-S1). For the flank cones, we measured the heights considering the method of Favalli et al. (2009). The volumes of scoria cones and lava domes were calculated by different formulas suggested for the truncated cone shapes (Hasenaka and Carmichael, 1985; Riedel et al., 2003; Kervyn et al., 2012) (Tables 2 and 3). For the estimation of cone volume (V_{co}), among the various formulas suggested by different studies (Hasenaka and Carmichael, 1985; Riedel et al., 2003; Kervyn et al., 2012) (Supplementary Material Data-S1), the more commonly used one by Hasenaka and Carmichael (1985) was preferred for further interpretations. The bulk volumes were corrected by Dense Rock Equivalent (DRE) eruptive volumes (edifice volume x 0.40 (% bulk-juvenile) x 0.50 (% DRE-juvenile; Kereszturi et al., 2013a) (Tables 2 and 3). The slopes were obtained by both empirical formulas (e.g., Bemis and Ferencz, 2017) and the measurements on digital elevation models. The results of the latter method were considered for further interpretations (Tables 2 and 3).

Some additional parameters suggested for scoria cones (i.e., steep-sided-ness, flat-topped-ness, relative crater depth, and crater slope with error estimations; Bemis and Ferencz, 2017) were also calculated for both scoria cones and lava domes in the CAVP (Tables 2 and 3). The error limits of ratio-based parameters (i.e., steep-sided-ness, flat-topped-ness) were derived from the empirical formulas

suggested by Bemis and Ferencz (2017) (Tables 2 and 3). The ideal value of steep-sided-ness (S = $2H_{co}/(W_{co}-W_{cr})$ is 0.6 (31°) and corresponds to the traditional ratio of H_{co}/W_{co} (0.18; Porter, 1972; Wood, 1980a), whereas the ratio of 0.4 is the ideal for flat-topped-ness (F = W_{cr}/W_{co}). For further interpretations, we preferred to use these parameters against the traditional ratios, especially due to the fact that steep-sided-ness better represents the flank slopes (Bemis and Ferencz, 2017).

3.2. Fractal Analysis

Many natural phenomena including earthquakes, floods, and volcanoes obey power-law frequency-size statistics and hence are considered as fractal (self-similar) features (e.g., Gutenberg and Richter, 1944; Mandelbrot, 1975; Turcotte and Greene, 1993; Malamud and Turcotte, 1999; Legrand, 2002). The size of volcanic eruptions (i.e., Volcanic Explosivity Index), the spatial distribution of volcanic vents, size of scoria cones, and morphology of volcanic ash particles are the common examples of fractal sets in volcanology (e.g., Mazzarini and Armienti, 2001; Ersoy et al., 2007; Pérez-López et al., 2011; Uslular et al., 2015). Fractal systems (spatial distribution of volcanic vents in our case) are described by non-integer exponent of a power-law function (e.g., Mazzarini and D'Orazio, 2003; and references therein). One of the robust methods to calculate the fractal dimensions is the two-point correlation function method, for the population of N vents, which defines the correlation integral C_2 (l) as (Grassberger and Procaccia, 1983; Hentschel and Procaccia, 1983; Bonnet et al., 2001):

$$C_2(l)=\frac{1}{N^2}N_p(l), \quad (1)$$

where N_p (l) is the number of vent pairs (UTM coordinates) whose separation is less than a given length l. In this cumulative-frequency-based definition, C_2 (l) is considered as scaled with l in the form of l^{D_2} for the fractal set of vents, where D_2 is the correlation dimension. We hereafter prefer to use the term D_f to be consistent while describing the fractal dimension. If scaling holds in Eq. 1, D_f is calculated from the slope of a linear regression line in the log C_2 (l) vs. log(l) plot (e.g., Bonnet et al., 2001) (Table 4). The lower (L_{co}) and upper (U_{co}) cut-off values (Bonnet et al., 2001), which are the limits between which volcanoes have a fractal distribution, were determined and subsequently used for the interpretation related to the crustal mechanism (e.g., Mazzarini, 2004; Mazzarini and Isola, 2010).

3.3. Vent Spacing and Poisson Nearest Neighbor (PNN) Analysis

The coefficient of variation (CV) is mostly used to define homogeneity in the distribution of vents (i.e., CV $<$ 1, regular distribution; CV = 1, random or Poisson distribution; CV $>$ 1, clustering of vents; e.g., Mazzarini and Isola, 2010 and references therein). The space between volcanic vents is an important parameter for the understanding of crustal mechanisms (e.g., distribution of fractures) controlling vent spacing in the adjacent volcanic fields (e.g., Mazzarini, 2007; Mazzarini and Isola, 2010; Mazzarini et al., 2010; 2016). This parameter can be estimated by the Nearest Neighbor (NN) distance method (Clark and Evans, 1954) considering the average minimum distance between vents (Table 4). The NN method has been commonly used to quantify the spatial distribution of point-like features on Earth and also extraterrestrial settings including volcanic edifices (e.g., scoria and spatter cones; Bruno et al., 2006; Hamilton et al., 2010; Mazzarini et al., 2016; Hove et al., 2017). The PNN analysis, as a type of NN method (Baloga et al., 2007), is performed in the volcanic fields for the understanding of the spatial distribution of vents (Connor and Hill, 1995; Le Corvec et al., 2013a). Similarly, we applied this method by using the "Geological Image Analysis Software" (GIAS; Beggan and Hamilton, 2010) for the monogenetic clusters in the CAVP (Table 5). Details on the methodology for both PNN analysis and GIAS outputs can be found in Le Corvec et al. (2013a, and references therein). The basic parameters (e.g., convex hull, *R*, *c*, and skewness) are listed in Table 5. The convex hull is here defined as a polygon created by connecting the outermost volcanic vents (Hamilton et al., 2010; Le Corvec et al., 2013a). The statistical values *R* and *c*, similar to the CV, are the indication of homogeneity in the vent distribution. Ideally, *R* and *c* values for a population displaying Poisson distribution are 1 and 0, respectively. However, the more dispersed distributions compared to Poisson display R values $>$ 1, while the more clustered ones have R values $<$ 1 (Beggan and Hamilton, 2010; Le Corvec et al., 2013a). As they are sample-size dependent values, all related diagrams are created within the 2σ uncertainty to overcome this issue (Le Corvec et al., 2013a). The density of vent distribution can also be estimated by considering the ratio between the number of vents (*N*) and the area of the convex hull (Table 5) (Le Corvec et al., 2013a; Mazzarini et al., 2016).

3.4. Principal Component Analysis (PCA)

The PCA is the most common dimensionality reduction method that has been applied to the spatial data in different aspects of earth sciences (Demšar et al., 2013), including volcanology (Prima and Yoshida,

2010; Mazzarini et al., 2016; Unglert et al., 2016). The original variables are transformed into the new uncorrelated axes that are aligned parallel to the directions of maximum variance in the data (e.g., Demšar et al., 2013).

In this study, we considered the UTM coordinates of the vents as a pair of variables used in the PCA and followed the steps in Mazzarini et al. (2016) (Table 5). After the dataset is scaled to the barycenter (i.e., the origin of the new dataset is the average values of coordinates), the covariance matrix (Q) of *N* vents is estimated by:

$$Q=\begin{bmatrix}\mathrm{cov}(X,X) & \mathrm{cov}(X,Y)\\ \mathrm{cov}(X,Y) & \mathrm{cov}(Y,Y)\end{bmatrix}, \quad (2)$$

with

$$\mathrm{cov}(X,Y)=\sum_{i=1}^{N}\frac{(x_i-\bar{x})(y_i-\bar{y})}{N} \quad (3)$$

where x_i and y_i are the coordinate values of N vents and their mean values ($\bar{x}$ and $\bar{y}$) are zero as the dataset is translated to barycenter-scaled. The eigenvalues and vectors with the dominant azimuthal direction of the largest eigenvectors are also computed (Mazzarini et al., 2016).

We here aim to provide the shape characteristics of the monogenetic clusters in the CAVP using PCA. The eccentricity (ecc), for instance, relates the lengths of the first and second eigenvectors of the Q (close to 0 and 1 for circular or elliptical volcanic fields, respectively) (Table 5). The azimuthal direction of the first eigenvalue of the Q, which is also considered as a proxy for the field elongation (Table 5), represents the major trend of a long axis for the shape of volcanic fields (Mazzarini et al., 2016).

3.5. Vent-to-Vent Distance (VVD) Analysis

The preferred azimuthal orientation and/or the anisotropy in vent distribution can be statistically analyzed (e.g., two-point azimuth method, Lutz, 1986; the VVD, Mazzarini et al., 2016) to understand the possible relationship between the spatial vent distribution and the tectonic stress fields (e.g., Connor, 1990; Cebriá et al., 2011; Mazzarini et al., 2016; Hove et al., 2017). As the vents are considered to be aligned along the same dike or fault (e.g., Takada, 1994), the azimuth values between vents in the monogenetic clusters are measured. The total number of the segments in the observed set of vents can

be expressed as N(N-1)/2, where N is the total number of vents (Wadge and Cross, 1988). The rose diagrams and related histograms of azimuthal distribution in each cluster (Table 5) were used to determine the main peaks (the angular error is $\pm$ 3°) and also the angular dispersion ($\Delta\alpha$°; Mazzarini et al., 2016). The unimodal azimuth distribution with a well-defined peak and small dispersion suggests well-aligned vents, while the bimodal distribution with several peaks and large dispersion refers to a dispersed (or scattered) distribution of vents (Mazzarini et al., 2016).

3.6. Alignment Analysis

In addition to the shape and fractal characteristics of the spatial distribution of monogenetic vents that provide crucial information for the dike networks at the upper crustal level (e.g., Mazzarini, 2004; 2007; Mazzarini and Isola, 2010; Mazzarini et al., 2013), cone elongations and vent alignments are other two important parameters, especially for the understanding of dike orientations (e.g., Tibaldi, 1995; Le Corvec et al., 2013a; Muirhead et al., 2015). In this regard, we have used the morphologies of cones and domes to estimate the possible dike orientations in the upper crust using both observational and computational methods (Paulsen and Wilson, 2010; Le Corvec et al., 2013a; Muirhead et al., 2015). If the shape reliability of each cone/dome is 1 (probable), or 2 (likely) (Muirhead et al., 2015), and the cone/dome or crater axial ratio (long to short) is above 1.2 (Paulsen and Wilson, 2010), the cone/dome lineaments were recorded and interpreted as the strike of the dike feeding for that observed volcanic feature (Tibaldi, 1995; Muirhead et al., 2015). Additionally, the breaching direction of cones is considered as a possible indicator of feeder dyke orientation (Tibaldi, 1995; Muirhead et al., 2015), where the possible reason for breaching is the flow emittance rather than flank collapse or basal inclination (e.g., Németh et al., 2011).

The cone lineament data were further supported by the vent alignment analyses performed using the MATLAB script of Le Corvec et al. (2013a). Different alignment thicknesses (or width tolerance) were considered (i.e., 11 to 21 with 5 m intervals), which also correspond to the limit of A-grade reliability ($\leq$ 125 m) for the vent alignments suggested by (Paulsen and Wilson, 2010). Subsequently, the best regression lines for each thickness were automatically generated (Le Corvec et al., 2013a). The length tolerance of the alignment, however, is based on the observed cone distribution in each cluster (i.e., the observed mean distances must be less than the estimated ones; Le Corvec et al., 2013a; Muirhead et al., 2015) (Table 5). The alignments were accepted if three vents were aligned within the limits of length tolerance (Fig. 1 of Le Corvec et al., 2013a), and the trend of the regression line was within $\pm$ 15° of a cone elongation observed for at least one of the three vents (Paulsen and Wilson, 2010; Muirhead et al.,

2015). Additionally, each computed alignment for different thicknesses was displayed on digital elevation models and other map sources using QGIS (Quantum Geographical Information System, version 3.14.15), and those that have geologically suitable lineaments were selected. Moreover, the upper limit of the artifact (i.e., ratio of rejected alignments) in each analysis was taken as 10% (Le Corvec et al., 2013a), and hence the best maximum distance for the generation of alignment was chosen from those having artifacts ≤10% and the higher number of alignments. In other words, the various alignment distances were computed for each monogenetic cluster, but the one that has higher accepted alignments (geologically) and lower artifacts (accepted vs. rejected alignments) was selected as the best maximum distance (Table 5; Supplementary Material Data-S2). In addition, the local and regional fault directions compiled and digitalized from the literature data (Pasquare et al., 1988; Toprak and Göncüoglu, 1993; Dhont et al., 1998; Froger et al., 1998; Genç and Yürür, 2010) were also displayed on rose diagrams (length weighted) created by using the QGIS plugin "Line Direction Histogram" (Tveite, 2015--2020) and compared with the vent and cone/dome alignments and the general extensional trend (N-S to NE-SW; e.g., Özsayın et al., 2013) in the CAVP.

4. Results

4.1. Morphological Characteristics

4.1.1. Scoria Cone Morphometry

The morphometric parameters of scoria cones (n = 174) are given in Supplementary Material Data-S1, and their mean values with 2σ standard errors for each monogenetic cluster can be found in Table 2. The number of measured scoria cones is the highest in cluster-5 and the lowest in cluster-2 (Table 2). Most of the studied scoria cones (n = 75) do not have a crater (amorphous type; Dóniz-Páez, 2015; Bemis and Ferencz, 2017). The gully and horseshoe-type cones are also abundant (n = 60; Supplementary Material Data-S1). However, ideal-type (Bemis and Ferencz, 2017) or A1-A2 symmetrical ring cones (Dóniz-Páez, 2015) are very rare (n = 13).

The mean width (or basal diameter) of the cones (W_{co}) is the largest in cluster-3 (723$\pm$69 m) and the smallest cluster-2 (536$\pm$87 m; Table 2). The mean height of the cones (H_{co}) changes from 48$\pm$9 m in cluster-2 to 90$\pm$8 m in cluster-1 (Table 2). However, the largest cone in the CAVP is located within cluster-6 (Mekedağ; the mean H_{co} and W_{co} values are 209 and 1621 m, respectively; Fig. 3 and Supplementary Material Data-S1). Almost half of the measured scoria cones in the CAVP have a crater, where the mean widths (W_{cr}) are the largest in cluster-6 (361$\pm$39 m) and smallest in cluster-5 (178$\pm$12

m; Table 2). The cluster-6 also has the deepest craters (H_{cr}; 43±5 m), but the lowest values belong to cluster-5 (14±1 m) and cluster-2 (11±3 m; Table 2). Slopes (S°) were measured on digital elevation models, and the mean values revealed that gently sloping cones (11.8±1.1°) were generally found in cluster-5, whereas the steepest ones were located at cluster-1 (16.4±0.8°) and cluster-6 (15.9±1.5°; Table 2). Clusters 3 and 6 have relatively higher DRE-corrected bulk volumes, whereas cluster-2 has a lower volume compared to other clusters (Table 2).

The morphometric parameters and their ratios (e.g., steep-sided-ness and flat-topped-ness; Table 2) were also presented in conventional binary plots for each monogenetic cluster with their comparison between each other and the age and volume (Fig. 3). Fig. 3A displays a relationship between the mean H_{co} and W_{co} of the scoria cones, and the slopes (i.e., H_{co}/W_{co}) obtained by the regression lines are all significantly below the so-called ideal (fresh cone) ratio (0.18; Wood, 1980a), except for a few that have greater or nearly equal ratios. However, the computed ratios seem to be consistent with more recently suggested ratios (0.098; Favalli et al., 2009). The cluster-5 displays the greatest variance in steep-sided-ness (S_{min} = 0.12; S_{max} = 0.64), while the clusters 1 and 6 have generally steep scoria cones (0.31±0.08 and 0.29±0.11, respectively; Table 2 and Fig. 3B). Flat-topped-ness (F = W_{cr}/W_{co}) values in cluster-6 (0.37±0.05) are very close to the ideal (fresh cone) ratio of 0.4 (Wood, 1980a), whereas those in other clusters vary from 0.23±0.05 to 0.31±0.05 (Table 2).

Fig 3B also illustrates that most of the steep-sided-ness and flat-topped-ness values are moderate, and there are only a few outliers that exceed the ideal ratios. There is no clear trend between these values and the edifice volumes (Figs. 3C and D). The compiled age data for the CAVP (Supplementary Material Data-S1) were also compared with the slopes measured by two different methods (i.e., digital elevation model-based slopes and formula-based steep-sided-ness values; Figs. 3E-F). There is no clear trend defined between slope and volume of scoria cones in each cluster. There might be some opportunity to investigate this possible relationship for the relatively older cones that display a negative trend in Figs. 3E-F, but the available geochronology data are not enough to support this claim.

4.1.2. Lava Dome Morphometry

The morphometric parameters of lava domes (n= 91) are given in Supplementary Material Data-S1, and their mean values with 2σ standard errors for each monogenetic cluster are summarized in Table 3. Lava domes are only found in four monogenetic clusters (1 to 4), as clusters 5 and 6 are mainly basaltic monogenetic fields (Fig. 1B). Lava domes are most abundant in cluster-1 (n = ~100; Table 1), and hence

the number of measured domes is highest there (n = 56; Table 3). They were also examined in terms of morphological diversity (Blake, 1990; Fink and Griffiths, 1998), and most of them are either platy or spiny (or Pelèan) with many representative examples of lobate and coulèe types (Fig. 2; Supplementary Material Data-S1). However, some lava domes display complex morphologies, such as the Nenezidağ lava dome in cluster-2 (92±4 ka; Türkecan et al., 2004 and references therein) with its both spiny and lobate morphology. Dikkartın lava dome in cluster-1 (10.1±0.8 ka; Sarıkaya et al., 2019) is one of the best examples for coulèe type (Fig. 2). Lava domes also create ridges consisting of aligned spiny domes (e.g., on the flanks of Erciyes stratovolcano in cluster-1; Şen et al., 2003; Higgins et al., 2015), or dome complexes (e.g., Korudağ in cluster-2; 24.9±2.1 ka; Schmitt et al., 2011) (Figs. 1 and 2).

For the morphometric analysis of lava domes, we adopted the common parameters mostly used for scoria cones (Tables 2 and 3). The mean width (or basal diameter) of the domes (W_{do}) is the largest in cluster-3 (1443±168 m) and the smallest in cluster-4 (719±62 m; Table 3). The height of the domes (H_{do}) varies from 110±20 m in cluster-4 to 174±21 m in cluster-3 (Table 3). In Fig. 4A, the H_{do}/W_{do} ratios of each cluster were compared to those with ideal (fresh dome) value of 0.22 (Karatson et al., 2013) and references therein) and different morphologies (i.e., spiny, 0.18; coulèe, 0.17; low, 0.09; Aguirre-Díaz et al., 2006). A considerable number of domes are aligned with the ideal dome ratio, whereas the regression lines of each cluster are in between low and coulèe type domes (Fig. 4A). The lava domes in cluster-1 have the highest ratios close to the coulèe and spiny type domes, which is consistent with the observed examples and topography (i.e., flank domes). However, this ratio sharply decreases from clusters 2 and 3 (both 0.11) to cluster-4 (0.09) (Fig. 4A). Interestingly, the caldera-bearing volcanic fields (clusters 2 and 3) with numerous resurgent domes have similar ratios, but cluster-4 has the lowest, possibly due to a few low-type domes.

Similar to the scoria cones, the shape parameters of lava domes from each field were also compared (Fig. 4B). The ideal value of steep-sided-ness (*S* or flank slope) for scoria cones (0.6; Bemis and Ferencz, 2017) was converted by considering the ideal H_{do}/W_{do} ratio of lava domes (Karatson et al., 2013 and references therein) to estimate an equivalent value (i.e., ~0.7). However, we kept the same ratio of W_{cr}/W_{co} (or flat-topped-ness "*F*" = 0.4; Wood, 1980a) as there is no suggested value for lava domes in the literature. For the measured lava domes, there are only a few that exceed the ideal ratio for flat-topped-ness, but most are located at the mid-range in terms of steep-sided-ness values (Fig. 4B). Clusters 1 to 4 have the steepest lava domes (0.38±0.07 and 0.35±0.08, respectively), whereas clusters 2 and 3 have more gently sloping domes (Table 3). In addition, there is a relatively positive correlation

between flat-topped-ness and steep-sided-ness parameters along with two different trends that might be linked with the age differences. The bulk volumes are almost identical in each cluster changing from 0.4 to 1.6 x 10^7 m^3 (Table 3). The volumes were also compared with the steep-sided-ness and flat-topped-ness, and there is a nearly positive trend especially for the steep-sided-ness (e.g., clusters 1 and 2; Figs. 4C and D). The geochronology data directly from lava domes in the CAVP are rather scarce, and hence it is almost impossible to investigate the possible slope differences between younger and older domes (Figs. 4E and F).

4.2. Self-Similar (Fractal) Clustering

The parameters obtained by the fractal analysis of Quaternary monogenetic vents in the CAVP are listed in Table 4. In addition to the fractal distribution of all vents in each cluster, scoria cones and lava domes in the CAVP were analyzed separately in terms of self-similar clustering (Table 4). A plateau in the slopes (i.e., local slope) of log C_2(l) vs. log (l) diagrams could not be well-defined for clusters 4 and 6 (Fig. 5), either due to the lesser number of vents or spatial distribution of vents or shape characteristics of the volcanic fields. The computed fractal dimensions D_f from the slope of log C_2(l) vs. log(l) plots for other clusters are: 1.16 (cluster-2); 1.48 (cluster-5); 1.55 (cluster-1); and 1.80 (cluster-3) (Table 4 and Fig. 5). On the other hand, the scoria cones and lava domes have D_f values of 1.40 and 1.13, respectively (Table 4). The error for the D_f values is almost negligible (i.e., R^2 = 0.99). The lower (L_{co}) and upper (U_{co}) cut-off values defined by the size ranges of each vent dataset are also given in Table 4. L_{co} values are very comparable in each cluster (0.5-0.8 km), while the U_{co} changes from 8.5 km (i.e., shallowest in cluster-3) to 16 km (i.e., deepest in cluster-5, Table 4 and Fig. 5). Clusters 1 and 2 have almost similar L_{co} (0.8 km) and U_{co} (10 km and 12 km, respectively) values.

4.3. Vent Spacing and Field Shape Characteristics

The maximum average vent spacing/separation is observed in cluster-3 (1676 m), while clusters 1 and 2 have the minimum values (939 m and 945 m, respectively; Table 4). The mean distances between the vents measured by the Poisson nearest neighbor analysis (not filtered) also reveal similar results (Table 5). The area of each cluster defined by a convex hull is also measured, and clusters 1 and 4 are the largest volcanic fields in the CAVP (8.68 x 10^8 and 8.55 x 10^8 m^2, respectively: Table 5). These convex hulls are also used for the density calculations (number of vents/m^2), revealing that the density of vents is highest in clusters 1 and 2 (2.13 x 10^{-7} and 2.39 x 10^{-7} m^2) and the lowest in clusters 3 and 4 (1.18 x

10^{-7} and 0.91 x 10^{-7} m^2; Table 5). The homogeneity indicators (i.e., coefficient of variation), or the short-range clustering, for the distribution of vents are generally equal or greater than 1 (i.e., clustered distribution; Table 4). However, the results of the Poisson nearest neighbor analysis show that clusters 1, 3, and 6 have a vent distribution fitting to the Poisson model (Table 5 and Fig. 7). Other clusters display clustered vent distributions (Table 5 and Fig. 7). Although most of the clusters in the CAVP are nearly circular ($\geq$ 0.70) based on the shape factor (short/long axes of ellipses drawn upon the convex hull), clusters 4 and 6 have more elongated shapes ($\leq$ 0.60; Table 5). As the convex hull shape is more sensitive to the outliers, the shape of volcanic fields is then discussed with the results of principal component and vent-to-vent distance analyses.

The field elongations (i.e., eccentricity) and the angular dispersion ($\Delta x°$) obtained by the principal component and vent-to-vent distance analyses do not show a clear relationship, except for cluster-1 (i.e., vents on the flanks of Erciyes stratovolcano) and the individual monogenetic fields (clusters 5 and 6) that display inverse relationship (i.e., increase in the angular dispersion with the decrease of eccentricity) (Table 6). All the monogenetic clusters have nearly circular elongations (i.e., eccentricity close to 0; Mazzarini et al., 2016; Table 6). In addition, the eccentricity increases from NE (i.e., 0.03 in cluster-1) through the middle part of the CAVP (i.e., 0.28 in cluster-4) towards the SW direction, and then again decreases through the SW-end of the region (i.e., 0.13 in cluster-6; Table 6; Fig. 7).

The main azimuthal trends of the vent distribution are compared in each cluster and also with the main fault zones in the CAVP (Fig. 7). In addition, we classify these azimuthal vent trends of each cluster as either normal (NW-SE) or sub-parallel (NE-SW), considering the general extensional direction of the CAVP (N0-90°E; Özsayın et al., 2013). Cluster-1 is the only exceptional case among the other clusters with its almost circular field shape and the radial vent patterns along the flanks of Erciyes stratovolcano (Şen et al., 2003) (Tables 5 and 6, and Fig. 7). The dominant azimuthal trend of the spatial vent distribution in cluster-1 is in the N7°E direction, consistent with the local tectonic stress (e.g., Toprak, 1998; Higgins et al., 2015). On the other hand, the trends in other clusters are generally sub-parallel, except cluster-2 that has a trend (N115°) almost normal to the main extensional direction. The latter is also parallel to the western border fault and perpendicular to the eastern border fault (Fig. 7). In addition, there is a clockwise rotation in the direction of vent alignments from cluster-2 to the southern parts (Table 6 and Fig. 7). However, this trend remains mostly constant in the southwestern ends of the CAVP.

4.4. Vent Alignments and Cone/Dome Elongations

The maximum distance to form the best alignment is determined considering the ratio of rejected alignments (i.e., 10% artifact; Le Corvec et al., 2013a) as illustrated in Supplementary Figure SF1. All detected alignments in clusters 3 (n=12) and 6 (n=7) are accepted, and therefore there is no artifact in these clusters. However, the number of rejected alignments in other clusters is high (Table 5 and Supplementary Figure SF1). The number of accepted alignments is highest in cluster-4 (n=49) and lowest in clusters 3 and 6 (Table 5). The most dominant trend in the vent alignments is along the NE-SW direction, which is sub-parallel to the main extensional direction (Fig. 7).

The dominant trend for the vent alignment in cluster-1 is N17-38°E (Fig. 7), but there are also vents and faults/lineaments with WNW-trend, which are parallel to the NW directed tensional fractures (Dhont et al., 1998). The main direction of vent alignments is normal to the regional extensional direction only in cluster-2, where there is a NW-SE to N-S trend sub-parallel to the western border fault (Fig. 7). In cluster-3, there is a similar trend of vent alignment with cluster-1, but some of the alignments are along with the main trend of Derinkuyu fault (Toprak and Kazmakçı, 1995) (Figs. 1B and 7). Similarly, cluster-4 has a dominant trend of N72-90°E with a relatively higher number of vents, possibly due to the accumulation of numerous vents (n = 25) in the eastern parts formed by the Plio-Quaternary activity of Keçiboyduran stratovolcano (Figs 1B and 2). In addition, the vents in its western part (i.e., Karataş basaltic field; Ercan et al., 1992; Aydar and Gourgaud, 1998) are oriented mostly in the NW-SE direction, sub-parallel to the western border fault (Fig. 7). Clusters 5 and 6 are almost identical in terms of dominant alignment trends, which are both sub-parallel to the direction of the eastern fault zone (also Ecemiş fault) and the regional extension (Fig. 7).

The elongations of cones and domes are almost identical in all clusters, sub-parallel to the regional extension direction (Fig. 7). The main trend is N70-90°E, except for cluster-6 where vents are aligned with the direction of N55-75°E (Fig. 7). The role of local and regional faults does not seem to be effective in the formation of cones/domes, but again there is an exception in cluster-6 where the elongation direction is almost parallel to the main direction of local faults and the eastern fault zone (also Ecemiş fault) (Fig. 7). The local extensional directions are relatively similar to the cone/dome elongations in clusters 3, 4, and 6 (Fig. 7).

5. Discussion

5.1. Morphological Implications

Morphological parameters of both scoria cones and lava domes display a scattered pattern in all binary plots (Figs. 3 and 4). Degradation can be one of the processes that result in this variation in the morphologies (e.g., Wood, 1980b; Hooper and Sheridan, 1998; Fornaciai et al., 2012; Kereszturi et al., 2012). Scoria cone degradation depending on different factors (e.g., time interval, climate) causes a progressive decrease in the morphological parameters of scoria cones compared to the theoretical parameters of an ideal fresh edifice (i.e., repose angle of 31˚, 0.6 steep-sided-ness, and 0.4 flat-topped-ness; Wood, 1980a; Bemis and Ferencz, 2017). This is also obvious in our results displayed in Fig. 3B, where most of the values plotted in the lower-left panel away from the ideal ratios. Fornaciai et al. (2012) suggested that there might be some accumulation of eroded materials at the flank of the cones due to the lack of any transporting agent (e.g., high precipitation in humid climatic conditions) that result in the larger enlargement of cone width (W_{co}) compared to crater width (W_{cr}). This type of erosion can therefore be observed in arid/semiarid climatic conditions (Fornaciai et al., 2012) that mostly characterize the Holocene conditions throughout the CAVP (e.g., Fontugne et al., 1999; Nemec and Kazancı, 1999). However, paleoclimatic conditions during Quaternary (at least up to the late Pleistocene) were much more humid with various lake environments (e.g., Erol, 1999; Kuzucuoğlu et al., 1999), when most of the cones/domes were formed. Therefore, it is a challenging task to directly ascribe the morphological variations to the paleoclimatic conditions in the CAVP.

Many other important factors affect the morphological variations: (i) the absence of initial ideal cone/dome as in the case of many volcanic fields (e.g., Kervyn et al., 2012; Bemis and Ferencz, 2017; Haag et al., 2019); (ii) the age discrepancies among the cones/domes and hence different erosional/degradational processes that can also be linked to local climatological conditions (e.g., Fornaciai et al., 2012); (iii) the different eruption styles and facies distribution in scoria cones (e.g., Valentine et al., 2007; Valentine and Gregg, 2008). Additionally, the average H_{co}/W_{co} ratio of all measured scoria cones is 0.08, which is within the limit of scoria cones formed in the extensional environments (Fornaciai et al., 2012). This result is in line with the well-known extensional tectonism in the CAVP (e.g., Toprak and Göncüoglu, 1993; Dhont et al., 1998; Genç and Yürür, 2010; Özsayın et al., 2013).

Despite some successful attempts towards the estimation of relative ages based on the cone morphometry (e.g., Inbar et al., 2011; Haag et al., 2019), the use of traditional morphometric ratios (e.g., H_{co}/W_{co}) mostly gives way to misleading interpretations due to the various internal and external effects that control the final morphology (e.g., Kereszturi et al., 2012; Kereszturi et al., 2013b). Therefore, here we only compared the formula and digital elevation model-based flank slopes of both scoria cones and lava domes with the available radiometric ages to check if there is any meaningful trend or not (Figs. 3E-F and 4E-F). However, there is no clear trend observed in the monogenetic clusters, possibly due to the intermittent magmatic activity or the lack of enough geochronology data to make a robust correlation.

5.2. Tectonomagmatic Controls on Spatial Vent Distribution

The spatial vent distribution is one of the best indications for the controlling mechanisms of the tectonic stress fields in volcanic fields (e.g., Takada, 1994; Le Corvec et al., 2013a; Muirhead et al., 2015; Hove et al., 2017; Haag et al., 2019). Therefore, the spatial distribution analysis of vents certainly provides new insights into the understanding of volcanological evolution and even risk assessments of the volcanic fields (e.g., Connor et al., 2000; Becerril et al., 2013; Mazzarini et al., 2013; Kósik et al., 2020). The eruptive volumes and the fissure lengths are also important indicators for the understanding of tectonomagmatic processes in volcanic fields (e.g., Valentine and Perry, 2007; Valentine et al., 2017). The shape of volcanic fields (i.e., convex hull; see Table 5) would also be the surface expression of the magma source in the mantle for scoria cones or in the crust for lava domes if the field elongations matched with the vent alignment directions (Le Corvec et al., 2013a). Half of the volcanic fields within the CAVP (clusters 4, 5, and 6) have a similar orientation of vent alignments and main field shapes (N88°E, N77°E, and N29°E respectively). This might indicate that the shallow and deep plumbing systems are mainly controlled by the crustal-scale structures (i.e., fractures). On the other hand, the shape orientations of other monogenetic clusters (cluster-2, N88°E; cluster-3, N133°) that do not match with the vent alignments are similar to the local extension directions, except for cluster-1 (N130°) consisting of almost radial patterns of monogenetic vents (Fig. 7). This exception is a common issue for the flank eruptions in the polygenetic volcanoes where the regional tectonic stress regime is overhelmed by the magmatic pressure (e.g., Nakamura, 1977). .

The Poisson nearest neighbor analysis reveals that half of the monogenetic clusters have a clustered distribution (clusters 1, 4, and 5), while the others display a vent distribution that fits the Poisson model (non-clustered; Fig. 6). The clustered vent distribution, especially in clusters 4 and 5, possibly indicates

the lateral extent of a partial melting zone in the upper mantle that propagates intermittent dike emplacements (e.g., Valentine and Hirano, 2010). This is also consistent with the existing partial melts in the heterogeneous upper mantle beneath these regions revealed by several geophysical anomalies (e.g., slow shear wave velocities in the upper mantle, Delph et al., 2017) and petrological implications (e.g., Gençalioğlu-Kuşcu and Geneli, 2010; Reid et al., 2017; Uslular and Gençalioğlu-Kuşcu, 2019a). Considering all other characteristics (e.g., small melting degree, small volume; Uslular et al., 2015; Reid et al., 2017; and this study), these volcanic fields are consistent with the low-flux tectonically controlled intraplate volcanic fields (Valentine and Perry, 2007). As for the non-clustered vent distributions (clusters 2, 3, and 6; Fig. 6), independent and short-lived shallow or deep magma reservoirs are the possible sources for the vent formation in these fields (e.g., Valentine and Hirano, 2010; Le Corvec et al., 2013a). The distinct geochemical characteristics of temporally successive (late Pleistocene to Holocene) lava dome activities in cluster-2 (Acıgöl caldera; Siebel et al., 2011) together with shallow upper cut-off depths (i.e., initial depth of dike intrusions) in these clusters (Table 4) support this claim. These fields have also both low-flux and low-rejuvenation magma activity (e.g., Le Corvec et al., 2013a). Regardless of the potential interpretations for vent clustering in CAVP, the presence of both clustered and non-clustered vent distribution is a good indication of the complexity in the geodynamical characteristics of the CAVP.

The main trends of cone elongations (almost E-W) in all clusters are sub-parallel to the regional extensional direction (N0-90°E; Fig. 7). However, the vent alignments are distinct and variable in each cluster (Fig. 7). Generally, there are two main preferred or dominant directions of vents defined in almost all the clusters in the CAVP (Fig. 7), that is also suitable with other volcanic regions related to strike-slip (or wrench) tectonism (e.g., Armenia, Pinacate; Le Corvec et al., 2013b, and references therein). However, the Kula volcanic field (e.g., Tokçaer et al., 2005; Şen et al., 2014), for instance, located within a pure extensional tectonic regime of western Anatolia shows clustered vent distribution with more than two main preferred orientations (Le Corvec et al., 2013a). The vents only in cluster-2 display almost an extension-normal alignment trend, whereas those in other clusters are aligned sub-parallel to the regional extension direction (Fig. 7). However, when the local extension trends are considered, clusters 3 and 5 have also extension-normal vents (Fig. 7).

The lineaments sub-parallel to the extension direction might indicate two main mechanisms for the emplacement of vents (e.g., Le Corvec et al., 2013a; Muirhead et al., 2015), namely pre-existing structures (e.g., Gudmundsson and Brenner, 2005; Valentine and Krogh, 2006; Le Corvec et al., 2013b)

and/or local rotations of extension direction (or σ_3; e.g., Pollard and Aydin, 1984; Muirhead et al., 2015). As for the CAVP these two mechanisms can be valid, but the latter case seems to be more prevalent as also supported by the structural and paleomagnetic surveys (e.g., block rotations, temporal changes in stress regime) in the region (Dirik and Göncüoglu, 1996; Dhont et al., 1998; Gürsoy et al., 1998; Platzman et al., 1998; Tatar et al., 2000; Piper et al., 2002). However, the role of pre-existing fractures is also apparent in the CAVP, especially revealed by the extension-normal vent alignments in cluster-2 (NW-SE to N-S) where the shortening trend of basement rocks before the late Miocene is NNW-SSE (Göncüoglu et al., 1994). Additionally, the vent and local fault alignments in clusters 3 and 5 are almost perpendicular to the local extension axes (Fig. 7). The radial vent pattern on the other hand, was solely observed in cluster-1 with the main trend of N17-38˚E (Fig. 7) as also inferred in the literature (Toprak, 1998; Şen et al., 2003; Higgins et al., 2015). The extension-sub-parallel trend of vent alignments in this cluster (N17-38˚E) as inferred in the literature (Toprak, 1998; Şen et al., 2003; Higgins et al., 2015) can be related to the local rotations of extension direction which is evident by the southward bending of the eastern border fault (i.e., lazy S to the rhomboidal pull apart basin, Dirik, 2001; Fig. 8). However, the radial pattern of spatial vent distribution is related to either the effects of the local stress field, probably caused by shallow magma reservoirs in the upper crust and also the mechanical interactions along the fault zones (e.g., Pollard and Aydin, 1984; Gudmundsson, 2006; 2012; Muirhead et al., 2012) and/or major volcano (or topographic) loading (e.g., Van Wyk de Vries and Merle, 1998; Muller et al., 2001; Acocella and Neri, 2009; Le Corvec et al., 2015). Considering the formation of volcanism in cluster-1 along the eastern border fault and also the existence of many indications for the shallow magma reservoirs beneath the region (Fig. 8), both mechanisms can be valid for the radial emplacement of vents. On the other hand, the trends of monogenetic clusters close to the western border fault have likely been affected by this fault zone, which exhibits a possible transition from dominantly strike-slip to normal dip-slip kinematics in southern parts of the CAVP. This is further supported by the N-S-aligned vents in cluster-5, which are parallel to the N-S trending normal faults of the western border fault zone, likely indicating a preference for E-W-directed extension in this region.

5.3. Geodynamical Perspectives: Special Reference to Crustal Structures

Central Anatolia is an important part of the escape tectonism in Anatolia possibly commenced at the late Miocene-early Pliocene (e.g., Şengör et al., 1985; Faccenna et al., 2006) when there is a westward extrusion of the Anatolian block along the North and East Anatolian fault zones (Fig. 1A) after the

collision between Arabian and Eurasian plates along the Bitlis suture zone during the middle Miocene (e.g., Şengör et al., 1985; Okay et al., 2010; Philippon et al., 2014; Cavazza et al., 2018). The initiation of widespread volcanism in the CAVP slightly postdates this collision based on the available geochronology data (i.e., Keçikalesi caldera, 13.7 $\pm$ 0.3 Ma; Besang et al., 1977) and has been directly influenced by the tectonic changes (Toprak and Göncüoglu, 1993; Dirik and Göncüoglu, 1996; Dhont et al., 1998; Froger et al., 1998; Toprak, 1998). The region has also been under the effect of continuing crustal deformation after the collision that resulted in crustal block rotations and temporal changes in the stress regime along central Anatolia (e.g., Tatar et al., 2000). The anticlockwise rotation of the southern part of the Anatolian block that was mostly juxtaposed to the CAVP was concentrated within the last 1-2 Ma (Tatar et al., 2000). This is well-correlated with the widespread volcanism in the CAVP during this time interval, possibly due to the tectonic changes in the border fault zone (e.g., the initiation of Quaternary volcanism in cluster-1, Toprak, 1998; Fig. 8). Hence, two border fault zones (e.g., Koçyiğit and Beyhan, 1998; Çemen et al., 1999) (Fig. 8) exert the main control for the widespread Plio-Quaternary volcanism in the CAVP, either by triggering the volcanism due to the stress changes (e.g., Gençalioğlu-Kuşcu and Geneli, 2010) or just being used as a pathway for the magma en-route to the surface (e.g., Toprak, 1998; Abgarmi et al., 2017). Considering all other implications, we here claim that the CAVP is a low-flux tectonically controlled volcanic field where the Quaternary volcanism is the passive response of the regional deformation (Valentine and Perry, 2007; Valentine and Hirano, 2010).

The mantle heterogeneity within the CAVP has been revealed by several petrological implications (e.g., (Reid et al., 2017; Uslular and Gençalioğlu-Kuşcu, 2019a). Together with small partial melts and small volume in the CAVP (e.g., Uslular et al., 2015; Reid et al., 2017), the lack of anomalous heat flow (except for the shallow Curie-depths especially in clusters 1, 2, and 3; Ateş et al., 2005) and the less evidence of geodynamic changes around the Plio-Quaternary (cf. Delph et al., 2017) indicates the long-lasting presence of partial melts in the heterogeneous mantle (e.g., Basin and Range; Valentine and Hirano, 2010). This is also a suitable scenario for the CAVP and its link with the collision to the east based on the recent petrology-oriented geodynamic models (e.g., Uslular and Gençalioğlu-Kuşcu, 2019a; Rabayrol et al., 2019). As for the possible triggering mechanism, the intra-continental faults that can project to the base of the lithosphere result in the decompression melting with batch modeling processes (e.g., Cas et al., 2017; Valentine et al., 2017). Therefore, considering the evidence of decompression melting (Gençalioğlu-Kuşcu and Geneli, 2010), the conflicts in the possible mechanisms of asthenospheric upwelling in the CAVP (e.g., Delph et al., 2017; Rabayrol et al., 2019), and the changes in regional stress fields (e.g., Tatar et al., 2000), the mechanism controlled by the lithospheric-scale Central Anatolian fault

zone (Fig. 8) can be a viable scenario for the evolution of Quaternary CAVP volcanism. Alternatively, this eastern border fault zone together with the western counterpart (i.e., Tuz Gölü fault zone) displaying various strike-slip structures (e.g., en-echelon structures, releasing bends; e.g., Dirik and Göncüoglu, 1996, Koçyiğit and Beyhan, 1998; Dirik, 2001) may have allowed the propagation of magma during the evolution of the CAVP (especially after late Pliocene).

The anticlockwise rotation of Anatolian block occurred in two successive temporal stages after the collision (i.e., crustal thickening up to the late Pliocene and subsequently the acceleration of rotation due to escape tectonics; e.g., Gürsoy et al., 1998; Tatar et al., 2000; Piper et al., 2002; Gürsoy et al., 2003). The strike-slip fault (or wrench) tectonism appears to be one the most suitable geodynamic models for the central Anatolia during the Quaternary period (e.g., Aydemir, 2009; Koçyiğit and Doğan, 2016). The vent alignments display azimuth distributions throughout the CAVP not directly linked to the regional anticlockwise rotation of the Central Analtolian block (Fig. 7). When the western border fault zone is considered as a boundary, the clusters in its northern parts display clockwise rotation in the vent alignments through cluster-4 which is almost juxtaposed to this fault zone (Fig. 7). However, this trend turns slightly anticlockwise in the southern part of the fault zone for the vent alignments of clusters 5 and 6 (Fig. 7). In addition to the possible role of the eastern border fault zone and the local faults, the southerly change in the direction of vent alignment may reflect the spatial variations in the characteristics of the western border fault zone that are also linked to the various crustal- and lithospheric-scale processes (e.g., crustal rotation and heating, tectonic escape, uplifting; Krystopowicz et al., 2020 and references therein). As for the cluster-1, both sub-parallel vent alignment to the direction of regional extension and the radial pattern of the spatial vent distribution proclaim that this part of the CAVP behaves like an immature rift zone (e.g., Acocella, 2014; Muirhead et al., 2015) where cluster-1 (Erciyes Volcanic Complex) may be the magmatic transfer zone. This claim is also supported by the vent alignments of clusters 2 and 3 (i.e., normal to the extension direction) that can be considered as the boundary between the so-called transfer zone (i.e., the eastern border fault zone) and the distal end of the so-called rift basin (i.e., the western border fault zone). The vent alignments in these regions are mainly controlled by the regional extensional stress fields (Muirhead et al., 2015). Similar to the vent alignments (Fig. 7), the spatial variation in the eccentricity values (i.e., field elongations; Table 5) also corroborates the above claim, and there is a significant increase in the eccentricity values from cluster-1 through clusters 2, 3, and 4, followed by the decrease throughout the southern ends of the CAVP. Such variation is well-documented in the main Ethiopian rift, for example, where the eccentricity values increase from the rift border to the main axis (Mazzarini et al., 2016).

Fig. 8 illustrates the probable crustal- and mantle dynamics beneath the CAVP. The type of interaction between lithospheric and asthenospheric mantle, i.e., either melt percolation (Rabayrol et al., 2019) or dripping (e.g., Göğüş et al., 2017; Reid et al., 2017) lies beyond the scope of this manuscript. However, the westward propagation of slab break-off in the sinking Arabian segment of the southern Neotethyan slab has mostly controlled the mid-Miocene to recent volcanism in the CAVP (e.g., Biryol et al., 2011; Cosentino et al., 2012; Schildgen et al., 2014; Rabayrol et al., 2019). This migration also resulted in uplift of southern central Anatolia and also significant changes in the retreat rates of the Cyprus (i.e., slowing) and Hellenic (i.e., speeding) trenches (e.g., Schildgen et al., 2014) (Fig. 1A). Interrelatedly, the dominant N-S convergence in the central Anatolia gave way to the NE-SW extension in the late Miocene (e.g., Özsayın et al., 2013; Schildgen et al., 2014), and its consequences together with the triggering of border fault zones via tectonic escape (i.e., change in the regional stress regime; Tatar et al., 2000) in the late Pliocene (e.g., Faccenna et al., 2006) directly controlled the widespread volcanism in the CAVP (e.g., Toprak and Göncüoglu, 1993; Dhont et al., 1998; Toprak, 1998; and this study). Within this scenario, the eastern border fault zone, which is situated at the near eastern boundary of the Inner Tauride suture zone (Fig. 1A), has a distinct role in the propagation of mantle-derived melts en-route to the surface and behaves like an immature rift zone together with the cluster-1 (i.e., magmatic transfer zone). This interpretation is well-documented in our multivariate statistical and alignment analysis of vents in the CAVP. On the other hand, the western border fault zone in the region has mostly played a role in the crustal propagation of the magma to the surface (e.g., Toprak and Göncüoglu, 1993; Dirik and Göncüoglu, 1996; and this study). Additionally, the spatial changes in the kinematics of this fault zone (i.e., changes from almost pure strike-slip in the NW to a transtensional in the SE; e.g., Krystopowicz et al., 2020) possibly shaped the vent alignments in the central (clusters 2 and 3) and southwestern parts (clusters 5 and 6) of the CAVP (Fig. 7).

The hot upper mantle with very slow shear velocities (≤4.2 km/s; Delph et al., 2017) beneath the CAVP has been well-documented (e.g., Biryol et al., 2011; Abgarmi et al., 2017; Reid et al., 2017; Artemieva and Shulgin, 2019). The low-velocity anomalies tentatively illustrated in Fig. 8 around 20 km (e.g., Abgarmi et al., 2017) display a good correlation with the widespread volcanism in the CAVP. The compiled earthquake data from central Anatolia (Supplementary Figure SF2) also indicate the possible depth of brittle-ductile transition as around 16-20 km (with the maximum events in 8-10 km) beneath the CAVP (Fig. 8). Additionally, we interpreted these anomalies as the possible depth of dike intrusions (or stalling magma reservoirs) with the results of our fractal analysis, considering the upper cut-off (U_{co}) values (Table 4; Fig. 5). Accordingly, these interpretations are well correlated with the available

geophysical studies and our analysis on the clustering of spatial vent distributions (i.e., clustered vs. non-clustered fields). For instance, the Curie depths are lower beneath the clusters 2 and 3 (≤10 km; Ateş et al., 2005) where U_{co} values are 12 and 8.5 km, respectively (Fig. 8). Also, the deepest U_{co} value of the cluster-5 (16 km) conforms with the Curie depths in this region (≥15 km; Ateş et al., 2005). A similar interpretation was not possible for clusters 4 and 6 due to the lack of acceptable local slopes in their fractal analysis (Fig. 5). Therefore, the depth of possible dike intrusions beneath the cluster-4 could only be adopted from a recent magnetotelluric study of (Tank and Karaş, 2020). On the other hand, there is no additional data for the KMF, and hence the possible depth could not be estimated. The variation of U_{co} values throughout the CAVP can also be an indication of different depths of magma reservoirs (e.g., shallower in the cluster-2 and deeper in the cluster-5). However, in both scenarios, crustal lithology (e.g., Hove et al., 2017) plays a critical role in controlling spatial differences in vent distributions in the CAVP (i.e., soft-substrata sedimentary basins in the south, Eregli plain, and Ulukışla basin, e.g., Clark and Robertson, 2005; Gürbüz et al., 2020; hard-substrata crystalline basement rocks in the north, namely Kırşehir block; Okay and Tüysüz, 1999).

6. Concluding Remarks

Our findings reveal that there is no significant correlation among the morphological parameters of scoria cones or lava domes, possibly due to the several factors (e.g., local climatological conditions, facies variations) that mostly shape their final morphologies. In addition, the intermittent magmatic activity and also the lack of sufficient geochronology data in the CAVP do not enable us to make any correlation between morphological parameters and the available ages.

The multivariate statistical analyses on both spatial distributions of vents and their alignments together with many other implications discussed in the literature proclaim that the CAVP is a tectonically-controlled intraplate volcanic field where the magmatism is driven by the regional deformations. The presence of both clustered and non-clustered vent distribution (also considering the petrological characteristics) reveals two different scenarios for the dike emplacement: the independent short-lived shallow (e.g., Nevşehir-Acıgöl volcanic field) or deep crustal magma reservoirs (e.g., Eğrikuyu monogenetic field) intermittently derived from a pre-existing melt-bearing heterogeneous mantle beneath the CAVP.

Within the strike-slip environment in the CAVP, the regional stress has been changed due to the crustal deformation that has continued since the Quaternary coeval with the widespread volcanism. This probably resulted in the triggering of the pre-existing melts in the upper heterogeneous mantle via lithospheric-scale Central Anatolian fault zone. Therefore, we here suggest that this fault zone behaves as a so-called immature rift zone in which the Erciyes volcanic field formed along this fault zone behaves as a magmatic transfer zone for the widespread Quaternary volcanism in the CAVP. On the other hand, the Tuz Gölü fault zone considered as the western border of a so-called rift basin in the CAVP possibly participates in the crustal propagation of magma en-route to the surface.

Acknowledgements

All graphs except for PNN and PCA analyses were prepared by using Veusz (python-based scientific plotting program; Sanders, 2008). We also acknowledge the freely available QGIS software that enabled us to create maps and perform some analysis (e.g., calculation of azimuth, drawing rose diagrams) using its comprehensive toolbox and various add-ins. We would like to thank Diana Roman for the editorial handling and the reviewers Greg Valentine and James D Muirhead for their constructive comments that mostly advanced the science of the manuscript.

Supplementary Material

Supplementary Data-S1. Morphological dataset of Quaternary scoria cones and lava domes in the CAVP

Supplementary Data-S2. Alignment analysis results for each MVFs in the CAVP

Supplementary Figure SF1

Supplementary Figure SF2

FIGURE CAPTIONS

Fig. 1A. Inset map showing the Neogene-Quaternary volcanics in the Anatolia (compiled from MTA 1/500000 scale geological maps) and the geographic location of the CAVP (modified after Uslular and Gençalioğlu-Kuşcu, 2019b and references therein); **B.** Distribution of Quaternary monogenetic vents in the CAVP (modified after Toprak, 1998; Arcasoy et al., 2004) displayed on a shaded digital elevation model (ALOS 3D World, 30 m x 30 m resolution). Fault dataset (compiled from Pasquare et al., 1988; Toprak and Göncüoglu, 1993; Dhont et al., 1998; Froger

et al., 1998; Genç and Yürür, 2010). IAESZ: İzmir-Ankara-Erzincan Suture Zone; ITSZ: Inner-Tauride Suture Zone; BSZ: Bitlis Suture Zone; EAFZ: East Anatolian Fault Zone; NAFZ: North Anatolian Fault Zone; CAFZ: Central Anatolian Fault Zone; DEF: Dündarlı-Erciyes Fault; DF: Derinkuyu Fault; KF: Keçiboyduran Fault. Numbers in parenthesis refer to each monogenetic cluster; Erciyes (EVC), Nevşehir-Acıgöl (NAVC), Derinkuyu (DVC), and Hasandağ-Keçiboyduran (HKVC) volcanic complexes, Eğrikuyu (EMF) and Karapınar (KMF) monogenetic fields.

Fig. 2. Quaternary monogenetic clusters in the CAVP displayed on the slope maps, and Google Earth images of the most representative monogenetic volcanoes from each cluster. Scoria cone morphologies were classified based on Dóniz-Páez (2015) and Bemis and Ferencz (2017). References for the fault dataset are as in Fig. 1. DEF: Dündarlı-Erciyes Fault; DF: Derinkuyu Fault; KF: Keçiboyduran Fault. See Fig. 1B for other abbreviations.

Fig. 3. Comparison of morphometric parameters of scoria cones from each monogenetic cluster. Dashed and colored lines in **A** are the regression lines displaying the slope (i.e. ratio) between H_{co} and W_{co}. Dashed lines in **B**, **C**, and **D** correspond to the ideal ratios (H_{co}/W_{co} = 0.18; W_{cr}/W_{co} = 0.4; Wood, 1980a). **E** and **F** display unclear trend (R^2 = 0.2-0.3) in between the mean slopes (i.e. steep-sided-ness and S°_{co}; Table 3) and the ages. See Fig. 1B for the abbreviations.

Fig. 4. Comparison of morphometric parameters of lava domes from each monogenetic cluster. Gray dashed lines in **A** are the regression lines displaying the ideal slopes (i.e. ratios) between H_{do} and W_{do} based on the different dome morphologies (i.e. general ratio = 0.22; coulèe-type = 0.18; Pelean-type = 0.17; low domes = 0.09; Blake, 1990; Aguirre-Díaz et al., 2006). Dashed lines in **B and C** correspond to the ideal ratios (H_{do}/W_{do} = 0.22 or *S* = 0.7; Karatson et al., 2013 and references therein; W_{cr}/W_{do} or *F* = 0.4; after Wood, 1980a). **E and F** display a rather scattered trend (R^2 = 0.2-0.3) in between the mean slopes (i.e. steep-sided-ness and S°_{do}; Table 3) and the ages. See Fig. 1B for the abbreviations.

Fig. 5. Logarithmic plots of *l*(m) vs. $C_2(l)$ displaying the fractal (*Df*) exponents. L_{co}: lower cut-off; U_{co}: upper cut-off. See text and Fig. 1B for the abbreviations.

Fig. 6. The number of vents in each monogenetic cluster vs. statistical values of *R* and *c* plots. Only cluster-3 fits Poisson model, but the other clusters reject the model and display a clustered distribution. See Fig. 1B for the abbreviations.

Fig. 7. Comparison of azimuth directions of spatial vent distribution and alignments with the cone/dome elongations and local and regional fault directions in each monogenetic cluster. Main azimuth trends shown by solid dashed lines were determined by the principal component analysis (i.e. azimuth of the first eigenvector). **N** is the total number of objects used in the analyses (i.e. accepted alignments, cone/dome, and faults). Local extensional axes were adopted from Dhont et al. (1998) and Genç and Yürür (2010). See Fig. 1B for the abbreviations.

Fig. 8. Simplified cross-sections (not to scale) along A-A' and B-B' profiles displaying the main crustal structures beneath the CAVP. The conceptual model for the interaction between the upwelling asthenosphere and sub-continental lithospheric mantle (SCLM) was adopted from Reid et al. (2017). See text for further discussions. Possible initial depths of dike intrusions beneath each monogenetic field are inferred from our fractal analysis (i.e. U_{co} values), except for cluster-4 where the local slope could not be defined (Fig.5), and hence the recent magnetotelluric imaging results (Türk and Karaş, 2020) were adopted. The low-velocity anomalies and possible Moho depth are from Abgarmi et al. (2017) and Vanacore et al. (2013), respectively. Faults illustrated in the Central Anatolian fault zone (CAFZ) are those of normal components. YF: Yeşilhisar fault. See Fig. 1B for other abbreviations.

Supplementary Figure SF1. Vent alignment analysis of monogenetic clusters based on the different thicknesses (11, 16, and 22 m). A. EVC (cluster-1); B. NAVC (cluster-2); C. HKVC (cluster-4); and D. EMF (cluster-5). The best representative alignment was chosen from those including artifacts $\leq 10\%$ and higher number of alignments. Styles of lines given as legend in C are valid for diagrams with other color codings. All computed alignments in clusters 3 and 6 were accepted, and hence there is no artifact in these clusters.

Supplementary Figure SF2. Earthquake dataset for the period of 2010-2019 around central Anatolia (compiled from the catalog of International Seismological Centre), revealing the possible thickness of the seismogenic (or brittle) layer beneath the central Anatolia.

REFERENCES

Abgarmi, B., Delph, J.R., Özacar, A.A., Beck, S.L., Zandt, G., Sandvol, E., Türkelli, N., Biryol, C.B., 2017. Structure of the crust and African slab beneath the central Anatolian plateau from receiver functions: New insights on isostatic compensation and slab dynamics. Geosphere 13, 1774–1787.

Acocella, V., 2014. Structural control on magmatism along divergent and convergent plate boundaries: Overview, model, problems. Earth-Sci. Rev. 136, 226–288.

Acocella, V., Neri, M., 2009. Dike propagation in volcanic edifices: overview and possible developments. Tectonophysics 471, 67–77.

Aguirre-Díaz, G.J., Carmen Jaimes-Viera, M. del, Nieto-Obregón, J., 2006. The Valle de Bravo Volcanic Field: Geology and geomorphometric parameters of a Quaternary monogenetic field at the front of the Mexican Volcanic Belt. In: Siebe, C., Macías, J.L., Aguirre-Díaz, G.J. (Eds.),. Geol. Soc. Am., pp. 139–154.

Arcasoy, A., 2001. A new method for detecting the alignments from point-like features: an application to the volcanic cones of Cappadocian Volcanic Province, Turkey (PhD thesis). Middle East Technical University, Ankara. 157p.

Arcasoy, A., Toprak, V., Kaymakçı, N., 2004. Comprehensive trip Based Lineament Detection Method (COSBALID) from point-like features: a GIS approach. Comput Geosci. 30, 45–57.

Artemieva, I.M., Shulgin, A., 2019. Geodynamics of Anatolia: Lithosphere thermal structure and thickness. Tectonics 38, 4465–4487.

Asan, K., Kurt, H., 2011. Petrology and Geochemistry of Post-Collisional Early Miocene Volcanism in the Karacadağ Area (Central Anatolia, Turkey). Acta Geol. Sin. 85, 1100–1117.

Ateş, A., Bilim, F., Büyüksaraç, A., 2005. Curie point depth investigation of Central Anatolia, Turkey. Pure. Appl. Geophys. 162, 357–371.

Atıcı, G., Schmitt, A.K., Friedrichs, B., Sparks, S., Danišík, M., Yurteri, E., Gündoğdu, E.A., Schindlbeck-Belo, J., Çobankaya, M., Wang, K.-L., others, 2019. Ages and glass compositions for paired large-volume eruptions from the Acigöl volcanic complex, Cappadocia (Turkey). Med. Geo. Rev. 1, 167–178.

Aydar, E., Çubukçu, E., Ulusoy, I., Ersoy, O., Sen, E., Yürür, M.T., Ekmekçi, M., Atıcı, G., Atak, O., Kabadayı, E., Akın, L., 2011. Nevşehir kalderası'nın volkanolojik-petrolojik evriminin ve tektonizma-volkanizma ilişkisinin zaman ve mekan içinde incelenmesi. TÜBİTAK Project No. 108Y063 (in Turkish with English Abstact).

Aydar, E., Gourgaud, A., 1998. The geology of Mount Hasan stratovolcano, central Anatolia, Turkey. J. Volcanol. Geotherm. Res. 85, 129–152.

Aydar, E., Schmitt, A.K., Çubukçu, H.E., Akin, L., Ersoy, O., Sen, E., Duncan, R.A., Atıcı, G., 2012. Correlation of ignimbrites in the central Anatolian volcanic province using zircon and plagioclase ages and zircon compositions. J. Volcanol. Geotherm. Res. 213, 83–97.

Aydemir, A., 2009. Tectonic investigation of Central Anatolia, Turkey, using geophysical data. J. Appl. Geophys. 68, 321–334.

Aydin, F., Schmitt, A.K., Siebel, W., Sönmez, M., Ersoy, Y., Lermi, A., Dirik, K., Duncan, R., 2014. Quaternary bimodal volcanism in the Niğde Volcanic Complex (Cappadocia, central Anatolia, Turkey): age, petrogenesis and geodynamic implications. Contrib. Mineral. Petrol. 168, 1078.

Baloga, S., Glaze, L., Bruno, B., 2007. Nearest-neighbor analysis of small features on Mars: Applications to tumuli and rootless cones. J. Geophys. Res. Planets 112.

Bartol, J., Govers, R., 2014. A single cause for uplift of the Central and Eastern Anatolian plateau? Tectonophysics 637, 116–136.

Batum, I., 1978. Geology and petrography of Acıgöl and Göllüdağ volcanics at southwest of Nevşehir, central Anatolia (Turkey). Yerbilimleri 4, 70–88.

Becerril, L., Cappello, A., Galindo, I., Neri, M., Del Negro, C., 2013. Spatial probability distribution of future volcanic eruptions at El Hierro Island (Canary Islands, Spain). J. Volcanol. Geotherm. Res. 257, 21–30.

Beggan, C., Hamilton, C.W., 2010. New image processing software for analyzing object size-frequency distributions, geometry, orientation, and spatial distribution. Comput. Geosci. 36, 539–549.

Bemis, K.G., Ferencz, M., 2017. Morphometric analysis of scoria cones: the potential for inferring process from shape. Geol. Soc. Spec. Publ. 446, 61–100.

Besang, C., Eckhardt, F., Harre, W., Kreuzer, H., Müller, P., 1977. Radiometrische altersbestimmungen an Neogenen eruptivgesteinen der Türkei. Geol. Jahr. 25, 3–36.

Biryol, C.B., Beck, S.L., Zandt, G., Özacar, A.A., 2011. Segmented African lithosphere beneath the Anatolian region inferred from teleseismic P-wave tomography. Geophys. J. Int. 184, 1037–1057.

Blake, S., 1990. Viscoplastic models of lava domes. In: Fink, J. H. (Ed.), Lava Flows and Domes. Springer, pp. 88–126.

Bonnet, E., Bour, O., Odling, N.E., Davy, P., Main, I., Cowie, P., Berkowitz, B., 2001. Scaling of fracture systems in geological media. Rev. Geophys. 39, 347–383.

Brenna, M., Cronin, S.J., Nemeth, K., Smith, I.E., Sohn, Y.K., 2011. The influence of magma plumbing complexity on monogenetic eruptions, Jeju Island, Korea. Terra Nova 23, 70–75.

Bruno, B.C., Fagents, S., Hamilton, C.W., Burr, D., Baloga, S., 2006. Identification of volcanic rootless cones, ice mounds, and impact craters on Earth and Mars: Using spatial distribution as a remote sensing tool. J. Geophys. Res. Planets 111.

Cañón-Tapia, E., 2020. Influence of method selection on clustering analyses of point-like features: Examples from three zones of distributed volcanism. Geomorphology 354, 107063.

Cas, R., Van Otterloo, J., Blaikie, T., Van Den Hove, J., 2017. The dynamics of a very large intra-plate continental basaltic volcanic province, the Newer Volcanics Province, SE Australia, and implications for other provinces. Geol. Soc. Spec. Publ. 446, 123–172.

Cavazza, W., Cattò, S., Zattin, M., Okay, A.I., Reiners, P., 2018. Thermochronology of the Miocene Arabia-Eurasia collision zone of southeastern Turkey. Geosphere 14, 2277–2293.

Cebriá, J., Martín-Escorza, C., López-Ruiz, J., Morán-Zenteno, D., Martiny, B., 2011. Numerical recognition of alignments in monogenetic volcanic areas: Examples from the Michoacán-Guanajuato Volcanic Field in Mexico and Calatrava in Spain. J. Volcanol. Geotherm. Res. 201, 73–82.

Clark, M., Robertson, A., 2005. Uppermost Cretaceous–Lower Tertiary Ulukışla Basin, south-central Turkey: sedimentary evolution of part of a unified basin complex within an evolving Neotethyan suture zone. Sediment. Geol. 173, 15–51.

Clark, P.J., Evans, F.C., 1954. Distance to nearest neighbor as a measure of spatial relationships in populations. Ecology 35, 445–453.

Connor, C.B., 1987. Structure of the Michoacán-Guanajuato volcanic field, Mexico. J. Volcanol. Geotherm. Res. 33, 191–200.

Connor, C.B., 1990. Cinder cone clustering in the Trans Mexican Volcanic Belt: implications for structural and petrologic models. J. Geophys. Res-Sol. Ea. 95, 19395–19405.

Connor, C.B., Hill, B.E., 1995. Three nonhomogeneous Poisson models for the probability of basaltic volcanism: application to the Yucca Mountain region, Nevada. J. Geophys. Res-Sol. Ea. 100, 10107–10125.

Connor, C.B., Stamatakos, J.A., Ferrill, D.A., Hill, B.E., Ofoegbu, G.I., Conway, F.M., Sagar, B., Trapp, J., 2000. Geologic factors controlling patterns of small-volume basaltic volcanism: Application to a volcanic hazards assessment at Yucca Mountain, Nevada. J. Geophys Res-Sol. Ea. 105, 417–432.

Cosentino, D., Schildgen, T.F., Cipollari, P., Faranda, C., Gliozzi, E., Hudáčková, N., Lucifora, S., Strecker, M.R., 2012. Late Miocene surface uplift of the southern margin of the Central Anatolian Plateau, Central Taurides, Turkey. Bulletin 124, 133–145.

Çemen, I., Göncüoglu, M.C., Dirik, K., 1999. Structural evolution of the Tuzgölü basin in Central Anatolia, Turkey. J. Geol. 107, 693–706.

Çiner, A., Doğan, U., Yıldırım, C., Akçar, N., Ivy-Ochs, S., Alfimov, V., Kubik, P.W., Schlüchter, C., 2015. Quaternary uplift rates of the Central Anatolian Plateau, Turkey: insights from cosmogenic isochron-burial nuclide dating of the Kızılırmak River terraces. Quat. Sci. Rev. 107, 81–97.

Delph, J.R., Abgarmi, B., Ward, K.M., Beck, S.L., Özacar, A.A., Zandt, G., Sandvol, E., Türkelli, N., Kalafat, D., 2017. The effects of subduction termination on the continental lithosphere: Linking volcanism, deformation, surface uplift, and slab tearing in central Anatolia. Geosphere 13, 1788–1805.

Demšar, U., Harris, P., Brunsdon, C., Fotheringham, A.S., McLoone, S., 2013. Principal component analysis on spatial data: an overview. Ann. Am. Assoc. Geogr. 103, 106–128.

Dhont, D., Chorowicz, J., Yürür, T., Froger, J.-L., Köse, O., Gündoğdu, N., 1998. Emplacement of volcanic vents and geodynamics of Central Anatolia, Turkey. J. Volcanol. Geotherm. Res. 85, 33–54.

Di Giuseppe, P., Agostini, S., Manetti, P., Savaşçın, M.Y., Conticelli, S., 2018. Sub-lithospheric origin of Na-alkaline and calc-alkaline magmas in a post-collisional tectonic regime: Sr-Nd-Pb isotopes in recent monogenetic volcanism of Cappadocia, Central Turkey. Lithos 316, 304–322.

Dirik, K., 2001. Neotectonic evolution of the northwestward arched segment of the Central Anatolian Fault Zone, Central Anatolia, Turkey. Geol. Acta 14, 147–158.

Dirik, K., Göncüoglu, M.C., 1996. Neotectonic characteristics of central Anatolia. Int. Geol. Rev. 38, 807–817.

Doğan-Külahçı, G.D., Temel, A., Gourgaud, A., Varol, E., Guillou, H., Deniel, C., 2018. Contemporaneous alkaline and calc-alkaline series in Central Anatolia (Turkey): Spatio-temporal evolution of a post-collisional Quaternary basaltic volcanism. J. Volcanol. Geotherm. Res. 356, 56–74.

Dóniz, J., Romero, C., Coello, E., Guillén, C., Sánchez, N., García-Cacho, L., García, A., 2008. Morphological and statistical characterisation of recent mafic volcanism on Tenerife (Canary Islands, Spain). J. Volcanol. Geotherm. Res. 173, 185–195.

Dóniz-Páez, J., 2015. Volcanic geomorphological classification of the cinder cones of Tenerife (Canary Islands, Spain). Geomorphology 228, 432–447.

Druitt, T., Brenchley, P., Gökten, Y., Francaviglia, V., 1995. Late Quaternary rhyolitic eruptions from the Acigöl Complex, central Turkey. J. Geol. Soc. 152, 655–667.

Ercan, T., Tokel, S., Matsuda, J.-I., Ui, T., Notsu, K., Fujitani, T., 1992. Hasandağı-Karacadağ (Orta Anadolu) Kuvaterner Volkanizmasına İlişkin Yeni Jeokimyasal, İzotopik ve Radyometrik Veriler. Türkiye Jeoloji Kurultayı Bülteni 7, 8–21. (Turkish with English Abstact)

Erol, O., 1999. A geomorphological study of the Sultansazliği lake, central Anatolia. Quat. Sci. Rev. 18, 647–657.

Ersoy, O., Aydar, E., Gourgaud, A., Artuner, H., Bayhan, H., 2007. Clustering of volcanic ash arising from different fragmentation mechanisms using Kohonen self-organizing maps. Comput. Geosci. 33, 821–828.

Faccenna, C., Bellier, O., Martinod, J., Piromallo, C., Regard, V., 2006. Slab detachment beneath eastern Anatolia: A possible cause for the formation of the North Anatolian Fault. Earth Planet. Sci. Lett. 242, 85–97.

Favalli, M., Karátson, D., Mazzarini, F., Pareschi, M.T., Boschi, E., 2009. Morphometry of scoria cones located on a volcano flank: a case study from Mt. Etna (Italy), based on high-resolution LiDAR data. J. Volcanol. Geotherm. Res. 186, 320–330.

Fink, J.H., Griffiths, R.W., 1998. Morphology, eruption rates, and rheology of lava domes: Insights from laboratory models. J. Geophys. Res. B: Solid Earth. 103, 527–545.

Fontugne, M., Kuzucuoğlu, C., Karabiyikoğlu, M., Hatte, C., Pastre, J.-F., 1999. From pleniglacial to holocene: A ^{14}C chronostratigraphy of environmental changes in the Konya plain, Turkey. Quat. Sci. Rev. 18, 573–591.

Fornaciai, A., Favalli, M., Karátson, D., Tarquini, S., Boschi, E., 2012. Morphometry of scoria cones, and their relation to geodynamic setting: A DEM-based analysis. J. Volcanol. Geotherm. Res. 217, 56–72.

Friedrichs, B., Atıcı, G., Danišík, M., Atakay, E., Çobankaya, M., Harvey, J.C., Yurteri, E., Schmitt, A.K., 2020. Late Pleistocene eruptive recurrence in the post-collisional Mt. Hasan stratovolcanic complex (Central Anatolia) revealed by zircon double-dating. J. Volcanol. Geotherm. Res. 404, 107007.

Friedrichs, B., Atıcı, G., Danišík, M., Yurteri, E., Schmitt, A.K., 2021. Sequence modeling in zircon double-dating of early Holocene Mt. Erciyes domes (Central Anatolia). Quat. Geochronol. 61, 101129.

Froger, J.-L., Lénat, J.-F., Chorowicz, J., Le Pennec, J.-L., Bourdier, J.-L., Köse, O., Zimitoglu, O., Gündogdu, N., Gourgaud, A., 1998. Hidden calderas evidenced by multisource geophysical data; example of Cappadocian Calderas, Central Anatolia. J. Volcanol. Geotherm. Res. 85, 99–128.

Genç, Y., Yürür, M.T., 2010. Coeval extension and compression in Late Mesozoic–Recent thin-skinned extensional tectonics in Central Anatolia, Turkey. J. Struct. Geol. 32, 623–640.

Gençalioğlu-Kuşcu, G., 2011. Geochemical characterization of a Quaternary monogenetic volcano in Erciyes volcanic complex: Cora Maar (Central Anatolian volcanic province, Turkey). Int. J. Earth Sci. 100, 1967–1985.

Gençalioğlu-Kuşcu, G., Atilla, C., Cas, R.A., Kuscu, I., 2007. Base surge deposits, eruption history, and depositional processes of a wet phreatomagmatic volcano in Central Anatolia (Cora Maar). J. Volcanol. Geotherm. Res. 159, 198–209.

Gençalioğlu-Kuşcu, G., Geneli, F., 2010. Review of post-collisional volcanism in the Central Anatolian Volcanic Province (Turkey), with special reference to the Tepeköy Volcanic Complex. Int. J. Earth Sci. 99, 593–621.

Gençoğlu-Korkmaz, G., Asan, K., Kurt, H., Morgan, G., 2017. $^{40}Ar/^{39}Ar$ geochronology, elemental and Sr-Nd-Pb isotope geochemistry of the Neogene bimodal volcanism in the Yukselen area, NW Konya (Central Anatolia, Turkey). J. Afr. Earth Sci. 129, 427–444.

Germa, A., Connor, L.J., Cañon-Tapia, E., Le Corvec, N., 2013. Tectonic and magmatic controls on the location of post-subduction monogenetic volcanoes in Baja California, Mexico, revealed through spatial analysis of eruptive vents. Bull. Volcanol. 75, 782.

Gevrek, A.I., Kazancı, N., 2000. A Pleistocene, pyroclastic-poor maar from central Anatolia, Turkey: influence of a local fault on a phreatomagmatic eruption. J. Volcanol. Geotherm. Res. 95, 309–317.

Gómez-Vasconcelos, M.G., Luis Macías, J., Avellán, D.R., Sosa-Ceballos, G., Garduño-Monroy, V.H., Cisneros-Máximo, G., Layer, P.W., Benowitz, J., López-Loera, H., López, F.M., others, 2020. The

control of preexisting faults on the distribution, morphology, and volume of monogenetic volcanism in the Michoacán-Guanajuato Volcanic Field. Geol. Soc. Am. Bull. 132, 2455-2474.

Göğüş, O.H., Pysklywec, R.N., Şengör, A., Gün, E., 2017. Drip tectonics and the enigmatic uplift of the Central Anatolian Plateau. Nat. Commun. 8, 1–9.

Göncüoğlu, C., Dirik, K., Erler, A., Yalınız, K., 1994. Orta Anadolu Masifinin doğu bölümünün jeolojisi, Bölüm 4: Orta Anadolu Masifinin Sivas Baseni ile ilişkisi. TPAO, Report No., 3535, (unpublished)

Göncüoğlu, M., Toprak, V., 1992. Neogene and quaternary volcanism of central anatolia: A volcano-structural evaluation. Bul Section Volcanol, Société Géologique de France 26, 1–6.

Graettinger, A., 2018. Trends in maar crater size and shape using the global Maar Volcano Location and Shape (MaarVLS) database. J Volcanol Geotherm Res 357, 1–13.

Grassberger, P., Procaccia, I., 1983. Characterization of strange attractors. Phys. Rev. Lett. 50, 346.

Gudmundsson, A., 2006. How local stresses control magma-chamber ruptures, dyke injections, and eruptions in composite volcanoes. Earth Sci. Rev. 79, 1–31.

Gudmundsson, A., 2012. Magma chambers: Formation, local stresses, excess pressures, and compartments. J. Volcanol. Geotherm. Res. 237, 19–41.

Gudmundsson, A., Brenner, S.L., 2005. On the conditions of sheet injections and eruptions in stratovolcanoes. Bull. Volcanol. 67, 768–782.

Gutenberg, B., Richter, C.F., 1944. Frequency of earthquakes in California. Bull. Seismol. Soc. Am. 34, 185–188.

Gürbüz, E., Seyitoğlu, G., Güney, A., 2020. Late Cenozoic tectono-sedimentary evolution of the Ulukışla Basin: progressive basin development in south-central Turkey. Int. J. Earth Sci. 109, 345–371.

Gürsoy, H., Piper, J., Tatar, O., 2003. Neotectonic deformation in the western sector of tectonic escape in Anatolia: palaeomagnetic study of the Afyon region, central Turkey. Tectonophysics 374, 57–79.

Gürsoy, H., Piper, J., Tatar, O., Mesci, L., 1998. Palaeomagnetic study of the Karaman and Karapinar volcanic complexes, central Turkey: neotectonic rotation in the south-central sector of the Anatolian Block. Tectonophysics 299, 191–211.

Haag, M.B., Baez, W.A., Sommer, C.A., Arnosio, J.M., Filipovich, R.E., 2019. Geomorphology and spatial distribution of monogenetic volcanoes in the southern Puna Plateau (NW Argentina). Geomorphology 342, 196–209.

Hamilton, C.W., Fagents, S.A., Thordarson, T., 2010. Explosive lava–water interactions II: self-organization processes among volcanic rootless eruption sites in the 1783–1784 Laki lava flow, Iceland. Bull. Volcanol. 72, 469–485.

Hasenaka, T., Carmichael, I.S., 1985. The cinder cones of Michoacán–Guanajuato, central Mexico: their age, volume and distribution, and magma discharge rate. J. Volcanol. Geotherm. Res. 25, 105–124.

Hentschel, H., Procaccia, I., 1983. The infinite number of generalized dimensions of fractals and strange attractors. Physica. D-Nonlinear Phen. 8, 435–444.

Higgins, M., Schoenbohm, L.M., Brocard, G., Kaymakci, N., Gosse, J.C., Cosca, M.A., 2015. New kinematic and geochronologic evidence for the Quaternary evolution of the Central Anatolian fault zone (CAFZ). Tectonics 34, 2118–2141.

Hooper, D.M., Sheridan, M.F., 1998. Computer-simulation models of scoria cone degradation. J. Volcanol. Geotherm. Res. 83, 241–267.

Hove, J. van den, Grose, L., Betts, P.G., Ailleres, L., Van Otterloo, J., Cas, R.A., 2017. Spatial analysis of an intra-plate basaltic volcanic field in a compressional tectonic setting: South-eastern Australia. J. Volcanol. Geotherm. Res. 335, 35–53.

Inbar, M., Gilichinsky, M., Melekestsev, I., Melnikov, D., Zaretskaya, N., 2011. Morphometric and morphological development of Holocene cinder cones: a field and remote sensing study in the Tolbachik volcanic field, Kamchatka. J. Volcanol. Geotherm. Res. 201, 301–311.

Karatson, D., Telbisz, T., Harangi, S., Magyari, E., Dunkl, I., Kiss, B., Janosi, C., Veres, D., Braun, M., Fodor, E., others, 2013. Morphometrical and geochronological constraints on the youngest eruptive

activity in East-Central Europe at the Ciomadul (Csomád) lava dome complex, East Carpathians. J. Volcanol. Geotherm. Res. 255, 43–56.

Keller, J., 1974. Quaternary maar volcanism near Karapinar in Central Anatolia. Bull. Volcanol. 38, 378–396.

Kereszturi, G., Jordan, G., Németh, K., Dóniz-Páez, J.F., 2012. Syn-eruptive morphometric variability of monogenetic scoria cones. Bull. Volcanol. 74, 2171–2185.

Kereszturi, G., Németh, K., Cronin, S.J., Agustín-Flores, J., Smith, I.E., Lindsay, J., 2013a. A model for calculating eruptive volumes for monogenetic volcanoes–Implication for the Quaternary Auckland Volcanic Field, New Zealand. J. Volcanol. Geotherm. Res. 266, 16–33.

Kereszturi, G., Adelina, G., Marti, J., Németh, K., Doniz-Paez, J., 2013b. Evaluation of morphometry-based dating of monogenetic volcanoes–a case study from Bandes del Sur, Tenerife (Canary Islands). Bull. Volcanol. 75, 734.

Kervyn, M., Ernst, G., Carracedo, J.-C., Jacobs, P., 2012. Geomorphometric variability of "monogenetic" volcanic cones: evidence from Mauna Kea, Lanzarote and experimental cones. Geomorphology 136, 59–75.

Kocaarslan, A., Ersoy, E.Y., 2018. Petrologic evolution of Miocene-Pliocene mafic volcanism in the Kangal and Gürün basins (Sivas-Malatya), central east Anatolia: Evidence for Miocene anorogenic magmas contaminated by continental crust. Lithos 310, 392–408.

Koçyiğit, A., Beyhan, A., 1998. A new intracontinental transcurrent structure: The Central Anatolian Fault Zone, Turkey. Tectonophysics 284, 317–336.

Koçyiğit, A., Doğan, U., 2016. Strike-slip Neotectonic regime and related structures in the Cappadocia region: a case study in the Salanda basin, Central Anatolia, Turkey. Turk J. Earth Sci. 25, 393–417.

Koçyiğit, A., Erol, O., 2001. A tectonic escape structure: Erciyes pull-apart basin, Kayseri, central Anatolia, Turkey. Geol. Acta 14, 133–145.

Kósik, S., Bebbington, M., Németh, K., 2020. Spatio-temporal hazard estimation in the central silicic part of Taupo Volcanic Zone, New Zealand, based on small to medium volume eruptions. Bull. Volcanol. 82:50, 1-15.

Krystopowicz, N.J., Schoenbohm, L.M., Rimando, J., Brocard, G., Rojay, B., 2020. Tectonic geomorphology and Plio-Quaternary structural evolution of the Tuzgölü fault zone, Turkey: Implications for deformation in the interior of the Central Anatolian Plateau. Geosphere 16, 1107-1124

Kurokawal, K., Otsukil, K., Hasenaka, T., 1995. Michoacán-Guanajuato region of the Mexican Volcanic Belt. Geofis. Int. 34, 309–320.

Kuzucuoğlu, C., Atakay, E.G., Mouralis, D., Atıcı, G., Guillou, H., Türkecan, A., Pastre, J.-F., 2020. Geomorphology and tephrochronology review of the Hasandağ volcano (southern Cappadocia, Turkey). Med. Geo. Rev. 1–31.

Kuzucuoğlu, C., Bertaux, J., Black, S., Denefle, M., Fontugne, M., Karabiyikoğlu, M., Kashima, K., Limondin-Lozouet, N., Mouralis, D., Orth, P., 1999. Reconstruction of climatic changes during the Late Pleistocene, based on sediment records from the Konya Basin (Central Anatolia, Turkey). Geol. J. 34, 175–198.

Le Corvec, N., McGovern, P.J., Grosfils, E.B., Galgana, G., 2015. Effects of crustal-scale mechanical layering on magma chamber failure and magma propagation within the Venusian lithosphere. J. Geophys. Res. Planets 120, 1279–1297.

Le Corvec, N., Menand, T., Lindsay, J., 2013b. Interaction of ascending magma with pre-existing crustal fractures in monogenetic basaltic volcanism: an experimental approach. J. Geophys. Res. B: Solid Earth 118, 968–984.

Le Corvec, N., Spörli, K.B., Rowland, J., Lindsay, J., 2013a. Spatial distribution and alignments of volcanic centers: clues to the formation of monogenetic volcanic fields. Earth Sci. Rev. 124, 96–114.

Legrand, D., 2002. Fractal dimensions of small, intermediate, and large earthquakes. Bull. Seismol. Soc. Am. 92, 3318–3320.

Lorenz, V., 1975. Formation of phreatomagmatic maar–diatreme volcanoes and its relevance to kimberlite diatremes. In: Physics and Chemistry of the Earth. Pergamon, pp. 17–27.

Lorenz, V., 2007. Syn-and post-eruptive hazards of maar–diatreme volcanoes. J. Volcanol. Geotherm. Res. 159, 285–312.

Lutz, T.M., 1986. An analysis of the orientations of large-scale crustal structures: A statistical approach based on areal distributions of pointlike features. J. Geophys. Res. B: Solid Earth. 91, 421–434.

Malamud, B.D., Turcotte, D.L., 1999. Self-organized criticality applied to Nat. Hazards. 20, 93–116.

Mandelbrot, B.B., 1975. Les objets fractals: forme, hasard et dimension. Flammarion, 212 p.

Mazzarini, F., 2004. Volcanic vent self-similar clustering and crustal thickness in the northern Main Ethiopian Rift. Geophys. Res. Lett. 31.

Mazzarini, F., 2007. Vent distribution and crustal thickness in stretched continental crust: The case of the Afar Depression (Ethiopia). Geosphere 3, 152–162.

Mazzarini, F., Armienti, P., 2001. Flank cones at Mount Etna Volcano: do they have a power-law distribution? Bull. Volcanol. 62, 420–430.

Mazzarini, F., D'Orazio, M., 2003. Spatial distribution of cones and satellite-detected lineaments in the Pali Aike Volcanic Field (southernmost Patagonia): insights into the tectonic setting of a Neogene rift system. J. Volcanol. Geotherm. Res. 120, 291–305.

Mazzarini, F., Ferrari, L., Isola, I., 2010. Self-similar clustering of cinder cones and crust thickness in the Michoacan–Guanajuato and Sierra de Chichinautzin volcanic fields, Trans-Mexican Volcanic Belt. Tectonophysics 486, 55–64.

Mazzarini, F., Isola, I., 2010. Monogenetic vent self-similar clustering in extending continental crust: Examples from the East African Rift System. Geosphere 6, 567–582.

Mazzarini, F., Keir, D., Isola, I., 2013. Spatial relationship between earthquakes and volcanic vents in the central-northern Main Ethiopian Rift. J. Volcanol. Geotherm. Res. 262, 123–133.

Mazzarini, F., Le Corvec, N., Isola, I., Favalli, M., 2016. Volcanic field elongation, vent distribution, and tectonic evolution of a continental rift: The Main Ethiopian Rift example. Geosphere 12, 706–720.

Mouralis, D., Pastre, J.F., Kuzucuoglu, C., Türkecan, A., Atici, Y., Slimak, L., Guillou, H., Kunesch, S., 2002. Les complexes volcaniques Rhyolithiques quaternaires d'Anatolie centrale (Göllü Dag et Acigöl, Turquie): Genèse, instabilité, contraintes environnementales. Quaternaire 13, 219–228.

Muirhead, J.D., Airoldi, G., Rowland, J.V., White, J.D., 2012. Interconnected sills and inclined sheet intrusions control shallow magma transport in the Ferrar large igneous province, Antarctica. Geol. Soc. Am. Bull. 124, 162–180.

Muirhead, J.D., Kattenhorn, S.A., Le Corvec, N., 2015. Varying styles of magmatic strain accommodation across the East African Rift. Geochem. Geophys. Geosyst. 16, 2775–2795.

Muller, J.R., Ito, G., Martel, S.J., 2001. Effects of volcano loading on dike propagation in an elastic half-space. J. Geophys. Res. B: Solid Earth 106, 11101–11113.

Murcia, H., Borrero, C., Németh, K., 2019. Overview and plumbing system implications of monogenetic volcanism in the northernmost Andes' volcanic province. J. Volcanol. Geotherm. Res. 383, 77–87.

Nakamura, K., 1977. Volcanoes as possible indicators of tectonic stress orientation—principle and proposal. J. Volcanol. Geotherm. Res. 2, 1-16.

Nemec, W., Kazanci, N., 1999. Quaternary colluvium in west-central Anatolia: sedimentary facies and palaeoclimatic significance. Sedimentology 46, 139–170.

Németh, K., 2010. Monogenetic volcanic fields: Origin, sedimentary record, and relationship with polygenetic volcanism. In: What is a Volcano? GSA Special Paper vol. 470, 43.

Németh, K., Kósik, S., 2020. Review of Explosive Hydrovolcanism. Geosciences 10, 44.

Németh, K., Risso, C., Nullo, F., Kereszturi, G., 2011. The role of collapsing and cone rafting on eruption style changes and final cone morphology: Los Morados scoria cone, Mendoza, Argentina. Cent. Eur. J. Geosci. 3, 102–118.

Notsu, K., Fujitani, T., Ui, T., Matsuda, J., Ercan, T., 1995. Geochemical features of collision-related volcanic rocks in central and eastern Anatolia, Turkey. J. Volcanol. Geotherm. Res. 64, 171–191.

Okay, A.I., Tüysüz, O., 1999. Tethyan sutures of northern Turkey. Geol. Soc. Spec. Publ. 156, 475–515.

Okay, A.I., Zattin, M., Cavazza, W., 2010. Apatite fission-track data for the Miocene Arabia-Eurasia collision. Geology 38, 35–38.

Özsayın, E., Çiner, A., Rojay, B., Dirik, K., Melnick, D., Fernandez-Blanco, D., Bertotti, G., Schildgen, T.F., Garcin, Y., Strecker, M.R., others, 2013. Plio-Quaternary extensional tectonics of the Central Anatolian Plateau: a case study from the Tuz Gölü Basin, Turkey. Turk. J. Earth Sci. 22, 691–714.

Pasquare, G., Poli, S., Vezzoli, L., Zanchi, A., 1988. Continental arc volcanism and tectonic setting in Central Anatolia, Turkey. Tectonophysics 146, 217–230.

Paulsen, T. S., Wilson, T. J., 2010. New criteria for systematic mapping and reliability assessment of monogenetic volcanic vent alignments and elongate volcanic vents for crustal stress analyses. Tectonophysics 482, 16–28.

Pedrazzi, D., Martí, J., Geyer, A., 2013. Stratigraphy, sedimentology and eruptive mechanisms in the tuff cone of El Golfo (Lanzarote, Canary Islands). Bull. Volcanol. 75, 1–17.

Pérez-López, R., Legrand, D., Garduño-Monroy, V., Rodríguez-Pascua, M., Giner-Robles, J., 2011. Scaling laws of the size-distribution of monogenetic volcanoes within the Michoacán-Guanajuato Volcanic Field (Mexico). J. Volcanol. Geotherm. Res. 201, 65–72.

Philippon, M., Brun, J.-P., Gueydan, F., Sokoutis, D., 2014. The interaction between Aegean back-arc extension and Anatolia escape since Middle Miocene. Tectonophysics 631, 176–188.

Piper, J., Gürsoy, H., Tatar, O., 2002. Palaeomagnetism and magnetic properties of the Cappadocian ignimbrite succession, central Turkey and Neogene tectonics of the Anatolian collage. J. Volcanol. Geotherm. Res. 117, 237–262.

Platzman, E., Tapirdamaz, C., Sanver, M., 1998. Neogene anticlockwise rotation of central Anatolia (Turkey): preliminary palaeomagnetic and geochronological results. Tectonophysics 299, 175–189.

Pollard, D.D., Aydin, A., 1984. Propagation and linkage of oceanic ridge segments. J. Geophys. Res. B: Solid Earth 89, 10017–10028.

Porter, S.C., 1972. Distribution, morphology, and size frequency of cinder cones on Mauna Kea volcano, Hawaii. Geol. Soc. Am. Bull. 83, 3607–3612.

Pourteau, A., Sudo, M., Candan, O., Lanari, P., Vidal, O., Oberhänsli, R., 2013. Neotethys closure history of Anatolia: insights from 40Ar–39Ar geochronology and P–T estimation in high-pressure metasedimentary rocks. J. Metamorph. Geol. 31, 585–606.

Prima, O.D.A., Yoshida, T., 2010. Characterization of volcanic geomorphology and geology by slope and topographic openness. Geomorphology 118, 22–32.

Rabayrol, F., Hart, C.J., Thorkelson, D.J., 2019. Temporal, spatial and geochemical evolution of late Cenozoic post-subduction magmatism in central and eastern Anatolia, Turkey. Lithos 336, 67–96.

Reid, M., Delph, J., Cosca, M., Schleiffarth, W., Kuşcu, G.G., 2019. Melt equilibration depths as sensors of lithospheric thickness during Eurasia-Arabia collision and the uplift of the Anatolian Plateau. Geology 47, 943–947.

Reid, M.R., Schleiffarth, W.K., Cosca, M.A., Delph, J.R., Blichert-Toft, J., Cooper, K.M., 2017. Shallow melting of MORB-like mantle under hot continental lithosphere, Central Anatolia. Geochem. Geophys. Geosyst. 18, 1866–1888.

Riedel, C., Ernst, G., Riley, M., 2003. Controls on the growth and geometry of pyroclastic constructs. J. Volcanol. Geotherm. Res. 127, 121–152.

Rodriguez-Gonzalez, A., Fernandez-Turiel, J., Perez-Torrado, F.J., Gimeno, D., Aulinas, M., 2010. Geomorphological reconstruction and morphometric modelling applied to past volcanism. Int. J. Earth Sci. 99, 645–660.

Sanders, J., 2008. Veusz-a scientific plotting package.

Sarıkaya, M.A., Çiner, A., Zreda, M., Şen, E., Ersoy, O., 2019. Chlorine degassing constrained by cosmogenic ^{36}Cl and radiocarbon dating of early Holocene rhyodacitic lava domes on Erciyes stratovolcano, central Turkey. J. Volcanol. Geotherm. Res. 369, 263–275.

Schildgen, T.F., Yıldırım, C., Cosentino, D., Strecker, M.R., 2014. Linking slab break-off, Hellenic trench retreat, and uplift of the Central and Eastern Anatolian plateaus. Earth Sci. Rev. 128, 147–168.

Schleiffarth, W., Darin, M., Reid, M., Umhoefer, P.J., 2018. Dynamics of episodic Late Cretaceous–Cenozoic magmatism across Central to Eastern Anatolia: New insights from an extensive geochronology compilation. Geosphere 14, 1990–2008.

Schmitt, A.K., Danisik, M., Aydar, E., Şen, E., Ulusoy, I., Lovera, O.M., 2014. Identifying the volcanic eruption depicted in a neolithic painting at Catalhoyuk, Central Anatolia, Turkey. PLoS One 9.

Schmitt, A.K., Danišík, M., Evans, N.J., Siebel, W., Kiemele, E., Aydin, F., Harvey, J.C., 2011. Acigöl rhyolite field, Central Anatolia (part 1): high-resolution dating of eruption episodes and zircon growth rates. Contrib. Mineral. Petrol. 162, 1215–1231.

Settle, M., 1979. The structure and emplacement of cinder cone fields. Am. J. Sci. 279, 1089–1107.

Siebel, W., Schmitt, A.K., Kiemele, E., Danišík, M., Aydin, F., 2011. Acigöl rhyolite field, central Anatolia (part II): geochemical and isotopic (Sr–Nd–Pb, δ 18O) constraints on volcanism involving two high-silica rhyolite suites. Contrib. Mineral. Petrol. 162, 1233–1247.

Şen, E., 1997. Erciyes Stratovolkanı'nın (Orta Anadolu) volkanolojik ve petrolojik gelişiminin incelenmesi (Master's thesis). Hacettepe University, Ankara, 268p.

Şen, E., Aydar, E., Bayhan, H., Gourgaud, A., 2014. Alkali Bazalt ve Piroklastik Çökellerin Volkanolojik Özellikleri, Kula Volkanları, Batı Anadolu Volcanological Characteristics of Alkaline Basalt and Pyroclastic Deposits, Kula Volcanoes, Western Anatolia. Bull. Earth Sci. App. Res. Cent. Hacettepe Univ. 35, 219–232.

Şen, E., Kürkçüoğlu, B., Aydar, E., Gourgaud, A., Vincent, P.M., 2003. Volcanological evolution of Mount Erciyes stratovolcano and origin of the Valibaba Tepe ignimbrite (Central Anatolia, Turkey). J. Volcanol. Geotherm. Res. 125, 225–246.

Şengör, A., Görür, N., Şaroğlu, F., 1985. Strike-slip faulting and related basin formation in zones of tectonic escape: Turkey as a case study. In: Strike-slip deformation, basin formation and sedimentation. Spec. Pub. SEPM, pp. 227–264.

Tadono, T., Takaku, J., Tsutsui, K., Oda, F., Nagai, H., 2015. Status of "ALOS World 3D (AW3D)" global DSM generation. In: 2015 IEEE International Geoscience and Remote Sensing Symposium (IGARSS). IEEE, pp. 3822–3825.

Takada, A., 1994. The influence of regional stress and magmatic input on styles of monogenetic and polygenetic volcanism. J. Geophys. Res. B: Solid Earth 99, 13563–13573.

Tank, S.B., Karaş, M., 2020. Unraveling the electrical conductivity structure to decipher the hydrothermal system beneath the Mt. Hasan composite volcano and its vicinity, SW Cappadocia, Turkey. J. Volcanol. Geotherm. Res. 107048.

Tatar, O., Piper, J.D., Gürsoy, H., 2000. Palaeomagnetic study of the Erciyes sector of the Ecemiş Fault Zone: neotectonic deformation in the southeastern part of the Anatolian Block. Geol. Soc. Spec. Publ. 173, 423–440.

Tibaldi, A., 1995. Morphology of pyroclastic cones and tectonics. J. Geophys. Res. B: Solid Earth 100, 24521–24535.

Tokçaer, M., Agostini, S., Savascin, M.Y., 2005. Geotectonic setting and origin of the youngest Kula volcanics (western Anatolia), with a new emplacement model. Turk. J. Earth Sci. 14, 145–166.

Toprak, V., 1998. Vent distribution and its relation to regional tectonics, Cappadocian Volcanics, Turkey. J. Volcanol. Geotherm. Res. 85, 55–67.

Toprak, V., Göncüoglu, M., 1993. Tectonic control on the development of the Neogene-Quaternary central Anatolian Volcanic Province, Turkey. Geol. J. 28, 357–369.

Toprak, V., Kaymakçı, N., 1995. Determination of Stress Orientation Using Slip Lineation Data in Pliocene Ignimbrites around Derinkuyu Fault (Nevşehir). Turk. J. Earth Sci. 4, 39–47.

Turcotte, D., Greene, L., 1993. A scale-invariant approach to flood-frequency analysis. Stoch. Hydrol. Hydraul. 7, 33–40.

Türkecan, A., Kuzucuoğlu, C., Mouralis, D., Pastre, J., Atıcı, Y., Guillou, H., Fontugne, M., 2004. Upper Pleistocene volcanism and palaeogeography in Cappadocia, Turkey. TÜBİTAK Project No.101Y109, MTA Report No.10652.

Tveite, H., 2015--2020. The QGIS Line Direction Histogram Plugin, howpublished = http://plugins.qgis.org/plugins/LineDirectionHistogram/.

Ulusoy, İ., Diker, C., Şen, E., Aydın, E., Akkaş, E., Gümüş, E., Çubukçu, H.E., Erkut, V. 2020. Surface expressions of morphostructural features at Hasandağ stratovolcano on DEM datasets. Med. Geo. Rev. 1-17.

Unglert, K., Radić, V., Jellinek, A.M., 2016. Principal component analysis vs. self-organizing maps combined with hierarchical clustering for pattern recognition in volcano seismic spectra. J. Volcanol. Geotherm. Res. 320, 58–74.

Uslular, G., Gençalioğlu-Kuşcu, G., 2019a. Mantle source heterogeneity in monogenetic basaltic systems: A case study of Eğrikuyu monogenetic field (Central Anatolia, Turkey). Geosphere 15, 295–323.

Uslular, G., Gençalioğlu-Kuşcu, G., 2019b. Geochemical characteristics of Anatolian basalts: Comment on "Neogene uplift and magmatism of Anatolia: Insights from drainage analysis and basaltic geochemistry" by McNab et al. Geochem. Geophys. Geosyst. 20, 530–541.

Uslular, G., Gençalioğlu-Kuşcu, G., 2020. Orta Anadolu Maarlarının insansız Hava Araçları (iHA) Kullanılarak 3B Modellenmesi ve Morfolojik, Fiziksel ve Jeokimyasal Özelliklerinin Karşılaştırılması. no. 118Y360 TÜBİTAK 1002, 191 s, in Turkish (with English Abstract).

Uslular, G., Gençalioğlu-Kuşcu, G., Arcasoy, A., 2015. Size-distribution of scoria cones within the Eğrikuyu monogenetic field (Central Anatolia, Turkey). J. Volcanol. Geotherm. Res. 301, 56–65.

Valentine, G.A., Connor, C.B., 2015. Basaltic volcanic fields. In: McNutt, S. R., Houghton, B., Stix, J., Rymer, H., Sigurdsson, H. (eds.), The Encyclopedia of Volcanoes. Elsevier. Elsevier, pp. 423–439.

Valentine, G.A., Cortés, J.A., Wilcom, E., Smith, E.I., Rasoazanamparany, C., Johnsen, R., Briner, J.P., Harp, A.G., Turrin, B., 2017. Lunar crater volcanic field (reveille and pancake ranges, basin and Range Province, Nevada, USA). Geosphere 13, 391–438.

Valentine, G.A., Hirano, N., 2010. Mechanisms of low-flux intraplate volcanic fields—Basin and Range (North America) and northwest Pacific Ocean. Geology 38, 55–58.

Valentine, G.A., Krier, D.J., Perry, F.V., Heiken, G., 2007. Eruptive and geomorphic processes at the Lathrop Wells scoria cone volcano. J. Volcanol. Geotherm. Res. 161, 57–80.

Valentine, G.A., Krier, D., Perry, F.V., Heiken, G., 2005. Scoria cone construction mechanisms, Lathrop Wells volcano, southern Nevada, USA. Geology 33, 629–632.

Valentine, G.A., Krogh, K.E., 2006. Emplacement of shallow dikes and sills beneath a small basaltic volcanic center–The role of pre-existing structure (Paiute Ridge, southern Nevada, USA). Earth Planet. Sci. Lett. 246, 217–230.

Valentine, G.A., Perry, F.V., 2007. Tectonically controlled, time-predictable basaltic volcanism from a lithospheric mantle source (central Basin and Range Province, USA). Earth. Planet. Sci. Lett. 261, 201–216.

Valentine, G., Gregg, T., 2008. Continental basaltic volcanoes—processes and problems. J. Volcanol. Geotherm. Res. 177, 857–873.

Van Wyk de Vries, B., Merle, O., 1998. Extension induced by volcanic loading in regional strike-slip zones. Geology 26, 983–986.

Vanacore, E., Taymaz, T., Saygin, E., 2013. Moho structure of the Anatolian Plate from receiver function analysis. Geophys. J. Int. 193, 329–337.

Wadge, G., Cross, A., 1988. Quantitative methods for detecting aligned points: An application to the volcanic vents of the Michoacan-Guanajuato volcanic field, Mexico. Geology 16, 815–818.

White, J.D., Ross, P.-S., 2011. Maar-diatreme volcanoes: A review. J. Volcanol. Geotherm. Res. 201, 1–29.

Wilson, M., Tankut, A., Guleç, N., 1997. Tertiary volcanism of the Galatia province, north-west Central Anatolia, Turkey. Lithos 42, 105–121.

Wood, C.A., 1980a. Morphometric evolution of cinder cones. J. Volcanol. Geotherm. Res. 7, 387–413.

Wood, C.A., 1980b. Morphometric analysis of cinder cone degradation. J. Volcanol. Geotherm. Res. 8, 137–160.

Yıldırım, T., Özgür, R., 1981. Acıgöl kalderası. Jeo. Derg. 10, 59–70.

Yurteri, E., 2018. Erciyes stratovolkanında yer alan dasitik domların, dom akıntılarının ve domlarla ilgili piroklastik çökellerin petrolojik incelenmesi (Master's thesis). Hacettepe University, Ankara, 153p.

Göksu Uslular: Conceptualization, Methodology, Formal analysis, Investigation, Writing-Original Draft; **Nicolas Le Corvec:** Methodology, Software, Supervision, Writing-Review & Editing; **Francesco Mazzarini:** Methodology, Formal Analysis, Supervision, Writing-Review & Editing; **Denis Legrand:** Methodology, Supervision; **Gonca Kuşcu:** Supervision, Writing-Review & Editing

Dear Editor,

We declare that there is no conflict of interest for our revised manuscript entitled "Morphological and Multivariate Statistical Analysis of Quaternary Monogenetic Vents in the Central Anatolian Volcanic Province (Turkey): Implications for the Volcano-Tectonic Evolution" to be submitted as a research article to the Journal of Volcanology and Geothermal Research.

Göksu Uslular (Ph.D. candidate)

Department of Geological Engineering

Muğla Sıtkı Koçman University

TR48000 Kötekli-Muğla / Turkey

Tel: +90 252 211 5764

Fax: +90 252 211 1912

Email: goksuuslular@mu.edu.tr; goeksu.uslular@etu.unige.ch

Table 1. Summary of Quaternary monogenetic clusters in the CAVP (modified after Toprak, 1998). Age data are restricted to those directly related to monogenetic edifices, otherwise not considered.

Cluster Name	Edifice	Composition	Age (Ma)	Method	Alignment
EVC (1)	Lava Dome (100)	dacitic to rhyolitic	0.008-0.60	U-Th/He [a,b] ^{36}Cl [c] Ar-Ar [d]	radial with a dominant NE-SW trend
	Scoria Cone (40)	basaltic to andesitic	0.01-0.71	K-Ar [e]	
	Maar (1)	basaltic andesitic	0.13-0.35	K-Ar [f]	
	Undif. (44)				
NAVC (2)	Lava Dome (24)	andesitic to rhyolitic	0.02-0.17	U-Th/He [g] K-Ar [h]	N-S NW-SE
	Scoria Cone (10)	basaltic to andesitic	0.03-0.62	K-Ar [h]	
	Maar (6) *	basaltic trachyandesitic and rhyolitic	0.02	U-Th/He [g]	
	Tuff Ring (2) *	basaltic	0.08-0.11	K-Ar [h]	
	Undif. (28)				
DVC (3)	Lava Dome (30)	dacitic to rhyolitic	0.09-1.10	U-Pb [g] K-Ar [h]	N-S NE-SW
	Scoria Cone (28)	basaltic	0.15-0.49	Ar-Ar [i,j] K-Ar [h]	
	Maar (1)	Basaltic			
	Undif. (3)				
HKVC (4)	Lava Dome (11)	andesitic to rhyolitic	0.009-0.70	U-Th/He [k,l] Ar-Ar [i,j]	NW-SE NE-SW
	Scoria Cone (33)	basaltic	0.02-0.13	U-Pb [i] Ar-Ar [j,m] K-Ar [e, n, o]	
	Maar (1)	basaltic			
	Undif. (34)				
EMF (5)	Scoria Cone (110)	basaltic	0.07-2.60	Ar-Ar [j] K-Ar [e, n]	N-S NE-SW
	Maar (8)	basaltic	1.30	Ar-Ar [j]	NW-SE
	Tuff Ring (1)?	basaltic			
KMF (6)	Scoria Cone (17)	basaltic	0.16-0.50	Ar-Ar [j] K-Ar [n]	NE-SW
	Lava Dome (1)	andesitic			
	Maar (4) *	basaltic			
	Undif. (3)				

*including explosion craters. **a–** Friedrichs et al. (2021); **b–** Yurteri (2018); **c–** Sarıkaya et al. (2019); **d–** Higgins et al. (2015); **e–** Doğan-Külahçı et al. (2018); **f–** Gençalioğlu-Kuşcu (2011); **g–** Schmitt et al. (2011); **h–** Türkecan et al.

(2004); **i–** Aydin et al. (2014); **j–** Reid et al. (2017); **k–** Friedrichs et al. (2020); **l–** Schmitt et al. (2014); **m–** Aydar and Gourgaud (1998) and references therein; **n–** Notsu et al. (1995); **o–** Kuzucuoğlu et al. (2020).

Table 2. The mean morphometric parameters of scoria cones in each monogenetic cluster

Parameters*	Symbol	EVC (1)	NAVC (2)	DVC (3)	HKVC (4)	EMF (5)	KMF (6)
N. of cones	171/238	32	6	22	29	75	10
Cone height (m)	H_{co}	90±8	48±9	83±11	65±8	68±5	75±21
Cone width (m)	W_{co}	703±44	536±87	723±69	557±55	676±36	634±141
Crater diameter (m)	W_{cr}	195±17	236±53	269±41	269±23	178±12	361±39
Crater depth (m)	H_{cr}	26±3	11±3	28±5	22±4	14±1	43±5
Cone slope (°)	S_{co}	16.4±0.8	11.8±1.1	14.5±0.9	15.0±0.7	12.5±0.4	15.9±1.7
Bulk volume (m^3) [a,b]	V_{co}	6.6±1.3E+06	2.1±0.8E+06	8.1±2.3E+06	3.6±0.9E+06	5.7±1.1E+06	7.1±3.8E+06
Steep-sided-ness (S) [c]	$2H_{co}/(W_{co}-W_{cr})$ †	0.31±0.08	0.22±0.07	0.26±0.08	0.25±0.10	0.22±0.07	0.29±0.11
Flat-topped-ness (F) [c]	W_{cr}/W_{co} ‡	0.27±0.06	0.23±0.06	0.31±0.05	0.29±0.06	0.23±0.05	0.37±0.05
Relative crater depth [c]	H_{cr}/H_{co}	0.35±0.07	0.18±0.01	0.32±0.04	0.27±0.05	0.20±0.02	0.55±0.26
Crater slope [c]	$2D_{cr}/(W_{cr}-W_v)$	0.27±0.04	0.12±0.02	0.21±0.03	0.19±0.02	0.15±0.01	0.26±0.07
Elongation	$minW_{co}/maxW_{co}$	0.78±0.08	0.75±0.09	0.78±0.08	0.79±0.11	0.82±0.09	0.80±0.12
		0.84±0.20	0.78±0.31	0.84±0.20	0.89±0.32	0.86±0.41	0.83±0.15

* all are the mean values of mean measurements performed in four directions for each scoria cone (Supplementary Material Data-S1)

Errors are given as 2σ.

[a] Hasenaka and Carmichael (1985), $V_c = \pi H_{co}/12$ x $(W_{cr}^2+W_{cr}W_{co}+W_{co}^2)$

[b] Kereszturi et al. (2013b), DRE-correction = V_c x 0.4 (% bulk-juvenile) x 0.5 (% DRE-juvenile)

[c] Bemis and Ferencz (2017), W_v is the vent width and assumed to be 0 m

† $0.5[(2H_{co}+errH)/(W_{co}-W_{cr}-errW)-(2H_{co}-errH)/(W_{co}-W_{cr}+errW)]$

‡ $0.5[(W_{cr}+errW)/(W_{co}-errW)-(W_{cr}-errW)/(W_{co}+errW)]$; errH and errW are 30 m (resolution of digital elevation models)

Table 3. The mean morphometric parameters of lava domes in each monogenetic cluster

Parameters	Symbol	EVC (1)	NAVC (2)	DVC (3)	HKVC (4)
N. of domes	91/65	56	13	11	11
Dome height (m)	H_{do}	156±14	152±22	174±21	110±20
Dome width (m)	W_{do}	857±71	1160±96	1443±168	719±82
Crater diameter (m)	W_{cr}	215±28	316±101	501±203	150±29
Crater depth (m)	H_{cr}	18±2	27±8	47±24	17±6
Dome slope (°)	S_{do}	20.7±0.6	16.6±1.2	15.2±0.8	19.7±2.3
Bulk volume (m^3) [a,b]	V_{do}	1.6±0.4E+07	1.6±0.5E+07	0.4±0.2E+07	0.4±0.1E+07
Steep-sided-ness (S) [c]	$2H_{do}/(W_{do}-W_{cr})$ †	0.38±0.07	0.28±0.04	0.26±0.03	0.35±0.08
Flat-topped-ness (F) [c]	W_{cr}/W_{do} ‡	0.20±0.04	0.26±0.03	0.21±0.02	0.23±0.06
Relative crater depth [c]	H_{cr}/H_{do}	0.12±0.03	0.20±0.07	0.15±0.07	0.17±0.11
Crater slope [c]	$2D_{cr}/(W_{cr}-W_v)$	0.18±0.02	0.19±0.03	0.17±0.04	0.20±0.05
Elongation	$minW_{do}/maxW_{do}$	0.80±0.12 0.84±0.20	0.90±0.03 0.78±0.31	0.80±0.03 0.84±0.20	0.80±0.03 0.89±0.32

* all are the mean values of mean measurements performed in four directions for each lava dome (Supplementary Material Data-3). Errors are given as 2σ.
[a]modified after Hasenaka and Carmichael (1985), $V_{do} = \pi H_{do}/12 \times (W_{cr}^2+W_{cr}W_{do}+W_{do}^2)$
[b]Kereszturi et al. (2013b), DRE-correction = V_{do} x 0.4 (% bulk-juvenile) x 0.5 (% DRE-juvenile)
[c]modified after Bemis and Ferencz (2017), W_v is the vent width and assumed to be 0 m
† $0.5[(2H_{do}+errH)/(W_{do}-W_{cr}-errW)-(2H_{do}-errH)/(W_{do}-W_{cr}+errW)]$
‡ $0.5[(W_{cr}+errW)/(W_{do}-errW)-(W_{cr}-errW)/(W_{do}+errW)]$; errH and errW are 30 m (resolution of digital elevation models)

Table 4. The parameters of vent spacing and self-similar clustering

Cluster	N	s (m)	CV	c	*Df*	L_{co} (km)	U_{co} (km)	R^2
EVC (1)	185	939	1.15	2 x 10E-07	1.55	0.8	10.0	0.99
NAVC (2)	76	945	1.19	1 x 10E-05	1.16	0.8	12.0	0.99
DVC (3)	62	1676	0.81	4 x 10E-08	1.80	0.6	8.5	0.99
HKVC (4)	79	1212	1.42	-	-	-	-	-
EMF (5)	118	1138	0.96	3 x 10E-07	1.48	0.5	16.0	0.99
KMF (6)	25	1131	0.97	-	-	-	-	-
Vent Type								
Scoria Cone	238	-	-	2 x 10E-07	1.50	0.5	15.0	0.99
Lava Dome	165	-	-	4 x 10E-06	1.13	0.7	8.0	0.99

N: number of vents; s: average vent separation; CV: coefficient of variation; c: normalization constant; D_f: fractal exponent (D_2); L_{co}: lower cut-off; U_{co}: upper cut-off; R^2: coefficient of correlation

Table 5. The results of the PNN and vent alignment analysis for each monogenetic cluster in the CAVP

	Basic parameters	**EVC (1)**	**NAVC (2)**	**DVC (3)**	**HKVC (4)**	**EMF (5)**	**KMF (6)**
Measured NN parameters	Area Convex Hull (m^2)	8.68E+08	3.10E+08	4.59E+08	8.55E+08	8.11E+08	1.2E+08
	Density (vent/m^2)	2.13E-07	2.39E-07	1.18E-07	0.9. E-07	1.45E-07	2.05E-07
	Mean distance NN (m)	939	945	1676	1212	1138	1131
	Expected mean distance NN (m)	1083	1023	1739	1692	1311	1104
	Skewness	6.56	2.96	1.45	3.66	5.22	1.79
	Kurtosis	64.39	10.08	2.07	14.67	40.71	2.58
NN results relative to the Poisson model	R	0.87	0.94	0.96	0.71	0.87	1.03
	Distribution	Clustered	Poisson	Poisson	Clustered	Clustered	Poisson
	C	-3.46	-1.02	-0.60	-4.90	-2.74	0.92
	Model fit	Rejected	Significant	Significant	Rejected	Rejected	Significant
Alignment Analysis	Best max. distance (m)	1360	1552	5118	2606	3738	3291
	N. of alignments	26	29	12	49	28	7
	Artifact %	12	9.4	0	10	9.7	0
Shape Analysis	Short axis ellipse (m)	29,850	19,209	28,743	22,897	29,918	14,809
	Long axis ellipse (m)	37,202	27,707	31,780	51,705	49,882	15,856
	Short axis / Long axis	0.80	0.70	0.90	0.44	0.60	0.93

Table 6. VVD and PCA analysis of monogenetic clusters in the CAVP

Cluster	Δα (°)	α (°)	Ecc	Max. axis (km)	Min. axis (km)
EVC (1)	125	7	0.03	31	29
NAVC (2)	85	125	0.08	21	18
DVC (3)	60	43	0.20	20	20
HKVC (4)	100	74	0.28	30	23
EMF (5)	65	71	0.22	42	26
KMF (6)	70	75	0.13	17	13

Δα (°): azimuthal angular dispersion in the VVD histogram; α (°) azimuth of maximum axis of PCA ellipse; ecc: eccentricity of PCA ellipse; Max. & Min. axis: length of maximum and minimum axes of PCA ellipse

Highlights

- The spatial distribution of the vents displays a self-similar (fractal) clustering
- The Poisson nearest neighbor analysis shows the different depths of magma reservoirs in each monogenetic volcanic field
- The pre-existing fractures, the extensional axis of the regional stress tensor, and the local stress field variations are the main controlling mechanisms
- The Central Anatolian Fault zone is a possible magmatic transfer zone that mostly shapes the widespread volcanism in the region.

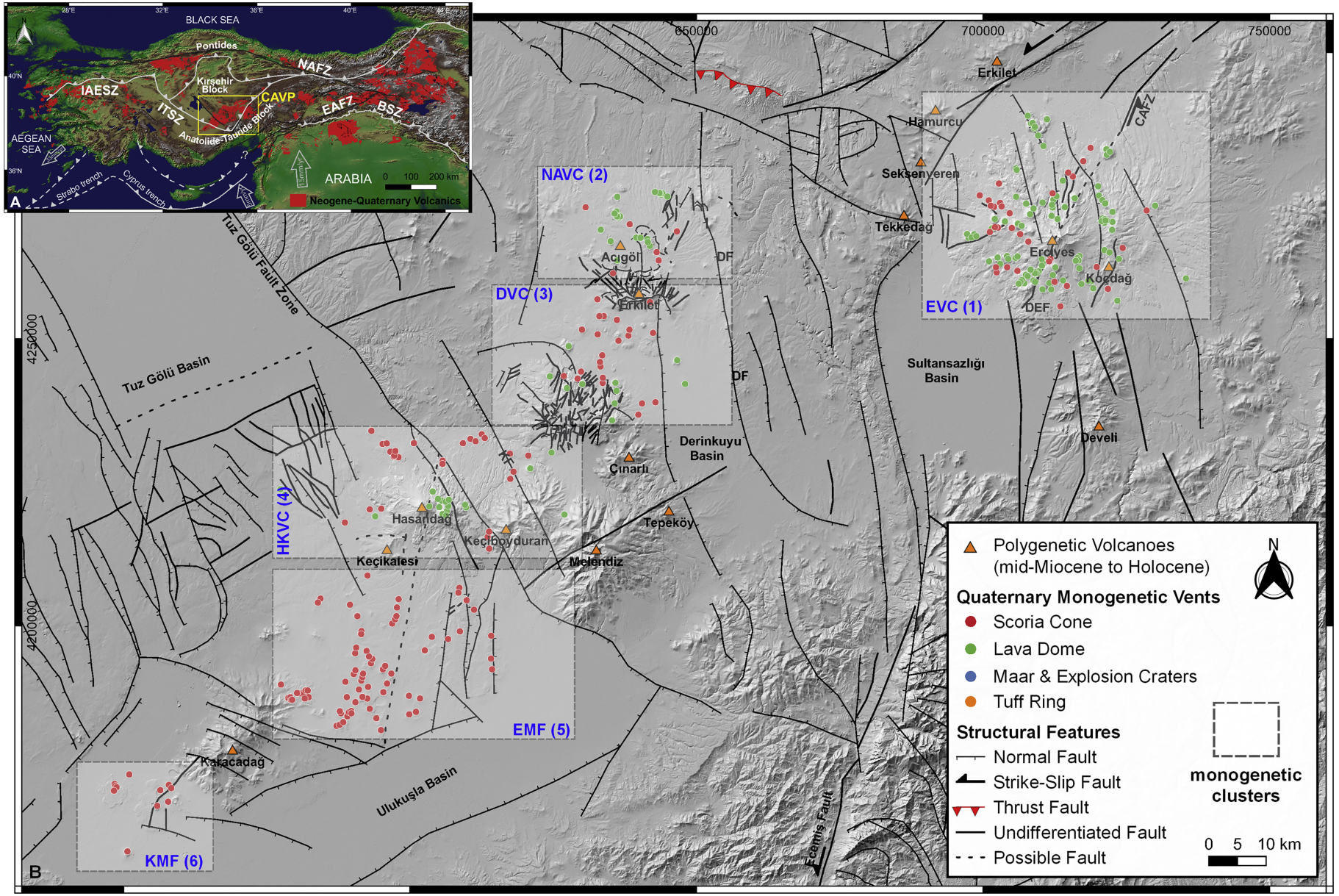
A
BLACK SEA
Pontides
NAFZ
Kirsehir Block
CAVP
IAESZ
ITSZ
Anatolide-Tauride Block
EAFZ
BSZ
AEGEAN SEA
Strabo trench
Cyprus trench
ARABIA
0 100 200 km
Neogene-Quaternary Volcanics
650000
700000
750000
4250000
4200000
Erkilet
Hamurcu
Seksenveren
Tekkedag
CAFZ
Acigöl
DF
NAVC (2)
DVC (3)
Erkilet
EVC (1)
Eroyes
Kocadag
DEF
Tuz Gölü Fault Zone
Tuz Gölü Basin
Sultansazlığı Basin
Derinkuyu Basin
Develi
Çınarlı
HKVC (4)
Hasandag
Keçiboyduran
Keçikalesi
Melendiz
Tepeköy
EMF (5)
Karacadag
Ulukuşla Basin
KMF (6)
Ecemis Fault
B
Polygenetic Volcanoes
(mid-Miocene to Holocene)
N
Quaternary Monogenetic Vents
Scoria Cone
Lava Dome
Maar & Explosion Craters
Tuff Ring
monogenetic clusters
Structural Features
Normal Fault
Strike-Slip Fault
Thrust Fault
Undifferentiated Fault
Possible Fault
0 5 10 km

Figure 1

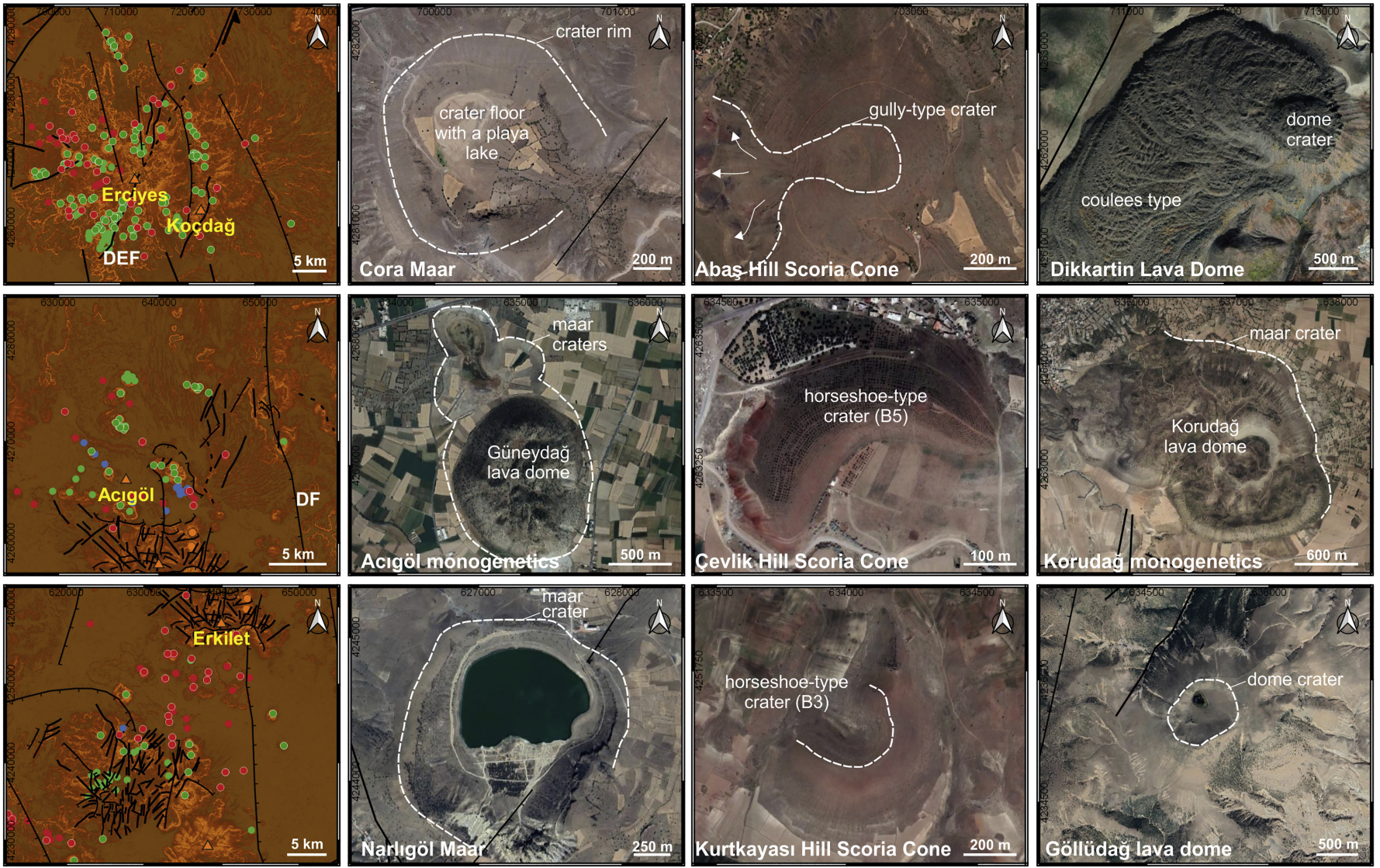
EVC (cluster 1)
NAVC (cluster 2)
DVC (cluster 3)
Erciyes
Koçdağ
DEF
5 km
crater rim
crater floor with a playa lake
Cora Maar
200 m
gully-type crater
Abaş Hill Scoria Cone
200 m
dome crater
coulees type
Dikkartin Lava Dome
500 m
Acıgöl
DF
5 km
maar craters
Güneydağ lava dome
Acıgöl monogenetics
500 m
horseshoe-type crater (B5)
Çevlik Hill Scoria Cone
100 m
maar crater
Korudağ lava dome
Korudağ monogenetics
600 m
Erkilet
5 km
maar crater
Narlıgöl Maar
250 m
horseshoe-type crater (B3)
Kurtkayası Hill Scoria Cone
200 m
dome crater
Göllüdağ lava dome
500 m

Figure 2A

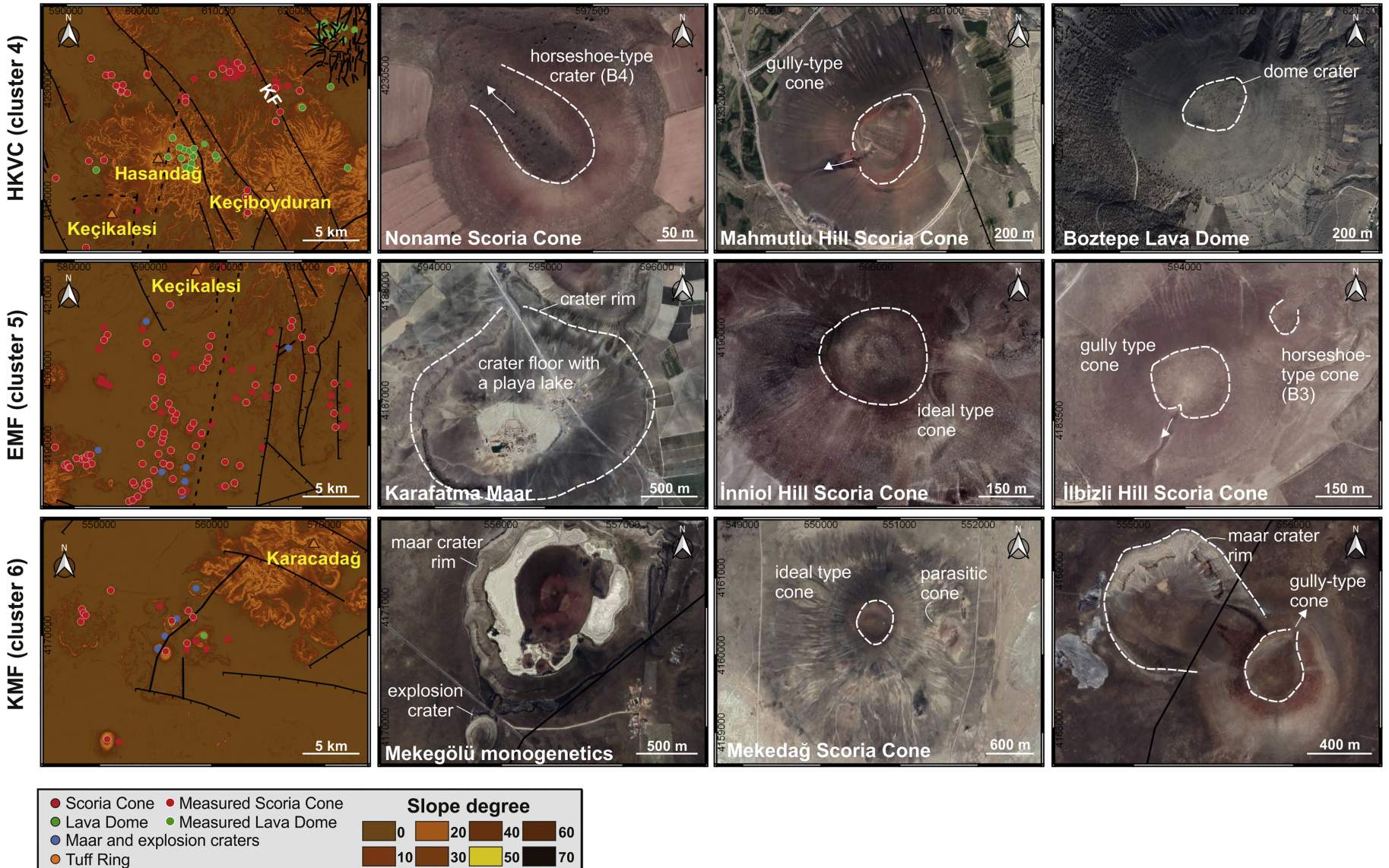
HKVC (cluster 4)
EMF (cluster 5)
KMF (cluster 6)
KF
Hasandağ
Keçiboyduran
Keçikalesi
5 km
horseshoe-type crater (B4)
Noname Scoria Cone
50 m
gully-type cone
Mahmutlu Hill Scoria Cone
200 m
dome crater
Boztepe Lava Dome
200 m
Keçikalesi
5 km
crater rim
crater floor with a playa lake
Karafatma Maar
500 m
ideal type cone
İnniol Hill Scoria Cone
150 m
gully type cone
horseshoe-type cone (B3)
İlbizli Hill Scoria Cone
150 m
Karacadağ
5 km
maar crater rim
explosion crater
Mekegölü monogenetics
500 m
ideal type cone
parasitic cone
Mekedağ Scoria Cone
600 m
maar crater rim
gully-type cone
400 m
Scoria Cone
Measured Scoria Cone
Lava Dome
Measured Lava Dome
Maar and explosion craters
Tuff Ring
Slope degree
0
10
20
30
40
50
60
70

Figure 2B

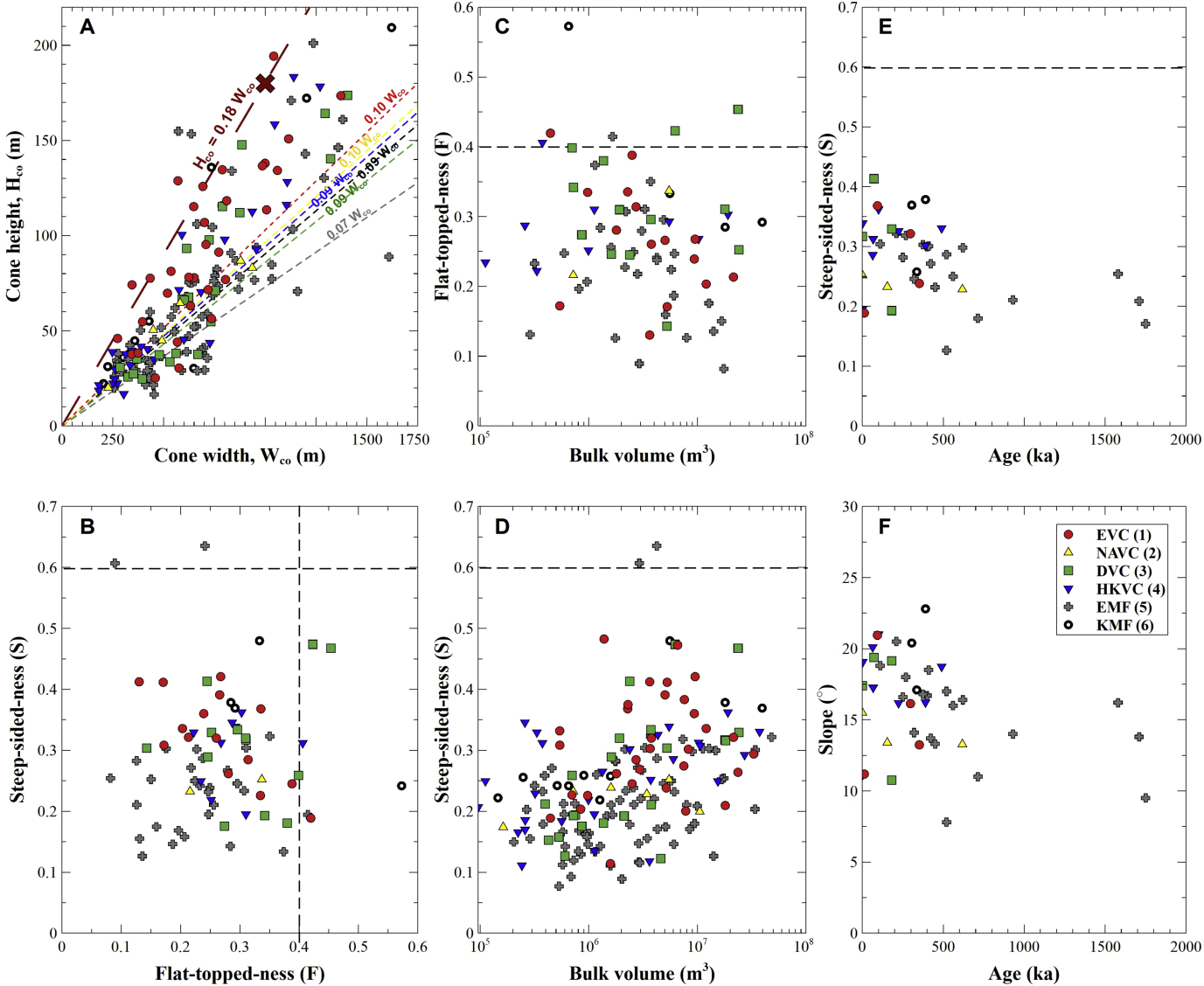
A
B
C
D
E
F
Cone height, H_{co} (m)
Cone width, W_{co} (m)
H_{co} = 0.18 W_{co}
0.10 W_{co}
0.10 W_{co}
0.09 W_{co}
0.09 W_{co}
0.07 W_{co}
Flat-topped-ness (F)
Bulk volume (m^3)
Steep-sided-ness (S)
Age (ka)
Slope (°)
EVC (1)
NAVC (2)
DVC (3)
HKVC (4)
EMF (5)
KMF (6)

Figure 3

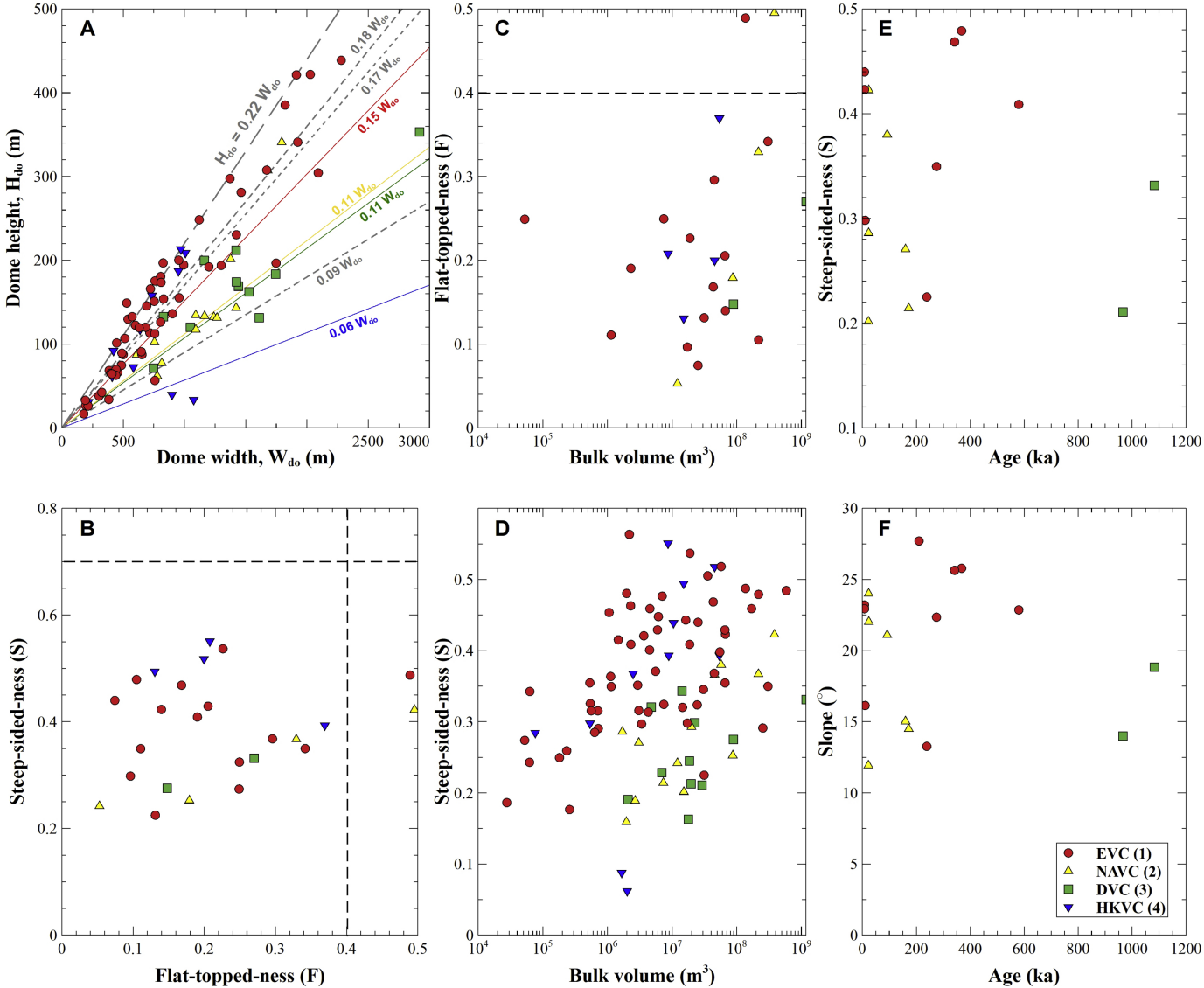
A
B
C
D
E
F
Dome height, H_{do} (m)
Dome width, W_{do} (m)
H_{do} = 0.22 W_{do}
0.18 W_{do}
0.17 W_{do}
0.15 W_{do}
0.11 W_{do}
0.11 W_{do}
0.09 W_{do}
0.06 W_{do}
Steep-sided-ness (S)
Flat-topped-ness (F)
Flat-topped-ness (F)
Steep-sided-ness (S)
Bulk volume (m^3)
Steep-sided-ness (S)
Bulk volume (m^3)
Steep-sided-ness (S)
Age (ka)
Slope (°)
Age (ka)
EVC (1)
NAVC (2)
DVC (3)
HKVC (4)

Figure 4

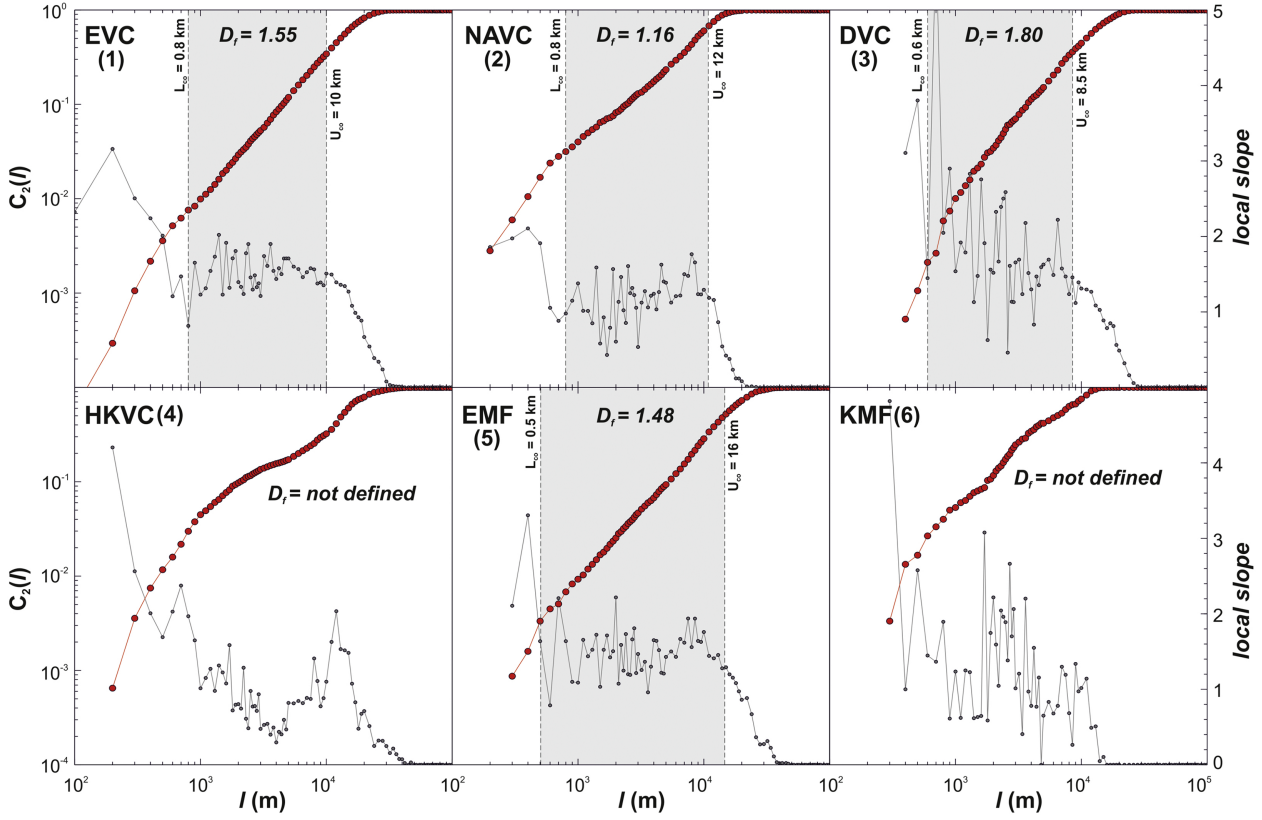
EVC
(1)
D_f = 1.55
L_∞ = 0.8 km
U_∞ = 10 km
NAVC
(2)
D_f = 1.16
L_∞ = 0.8 km
U_∞ = 12 km
DVC
(3)
D_f = 1.80
L_∞ = 0.6 km
U_∞ = 8.5 km
HKVC (4)
D_f = not defined
EMF
(5)
D_f = 1.48
L_∞ = 0.5 km
U_∞ = 16 km
KMF (6)
D_f = not defined
$C_2(l)$
local slope
l (m)

Figure 5

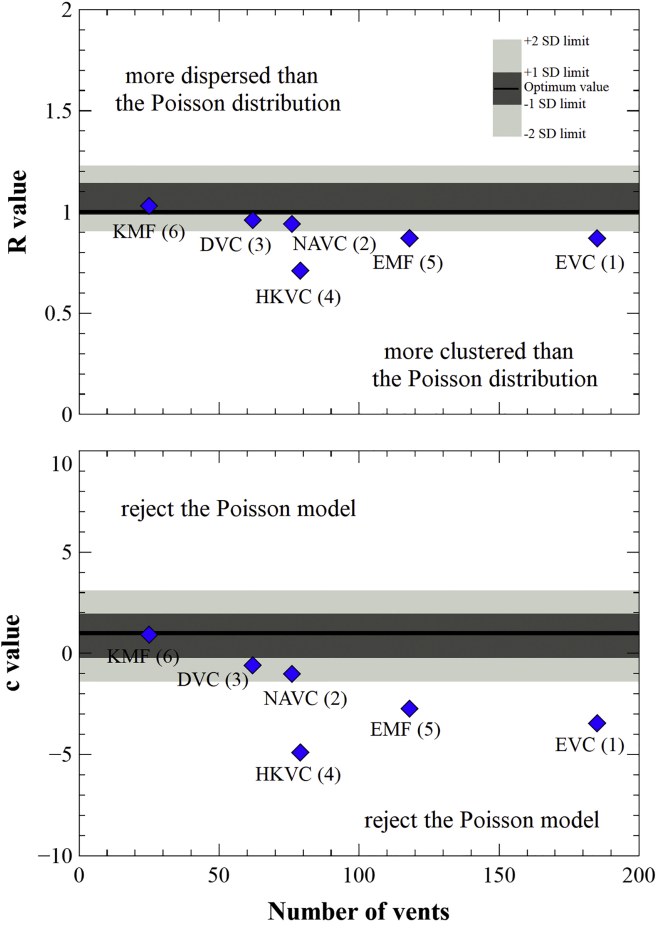
+2 SD limit
+1 SD limit
Optimum value
-1 SD limit
-2 SD limit
more dispersed than
the Poisson distribution
more clustered than
the Poisson distribution
R value
KMF (6)
DVC (3)
NAVC (2)
EMF (5)
EVC (1)
HKVC (4)
reject the Poisson model
reject the Poisson model
c value
KMF (6)
DVC (3)
NAVC (2)
EMF (5)
EVC (1)
HKVC (4)
Number of vents

Figure 6

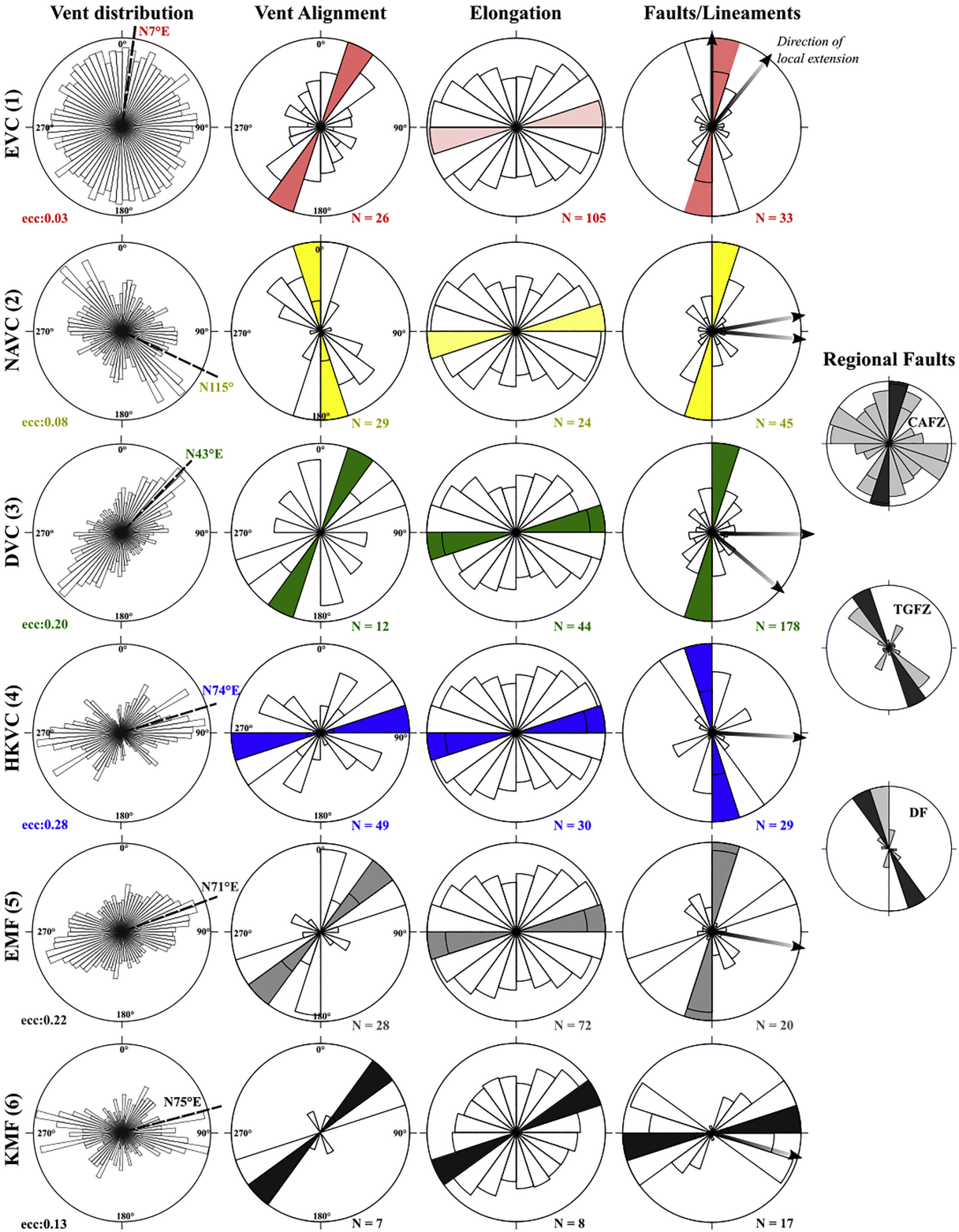
Vent distribution
Vent Alignment
Elongation
Faults/Lineaments
Direction of local extension
EVC (1)
N7°E
ecc:0.03
N = 26
N = 105
N = 33
NAVC (2)
N115°
ecc:0.08
N = 29
N = 24
N = 45
DVC (3)
N43°E
ecc:0.20
N = 12
N = 44
N = 178
HKVC (4)
N74°E
ecc:0.28
N = 49
N = 30
N = 29
EMF (5)
N71°E
ecc:0.22
N = 28
N = 72
N = 20
KMF (6)
N75°E
ecc:0.13
N = 7
N = 8
N = 17
Regional Faults
CAFZ
TGFZ
DF
0°
90°
180°
270°

Figure 7

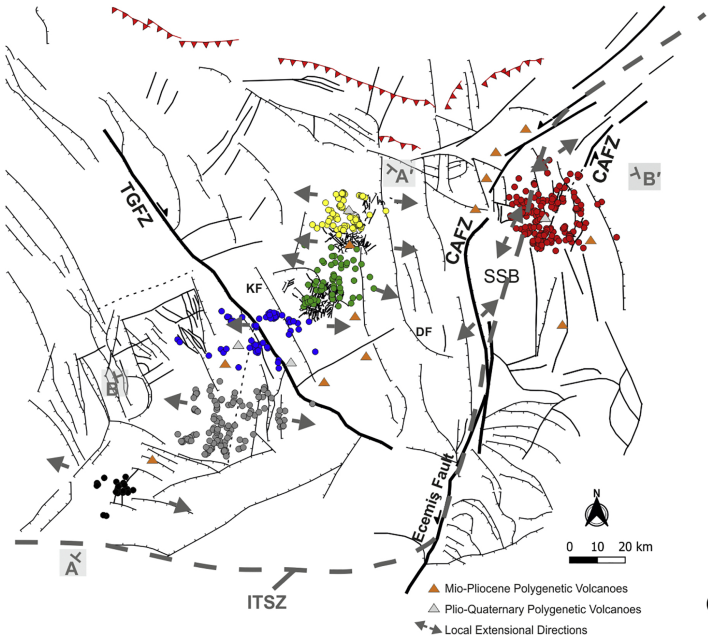
TGFZ
KF
DF
CAFZ
SSB
Ecemiş Fault
ITSZ
A
A'
B
B'
N
0 10 20 km
Mio-Pliocene Polygenetic Volcanoes
Plio-Quaternary Polygenetic Volcanoes
Local Extensional Directions

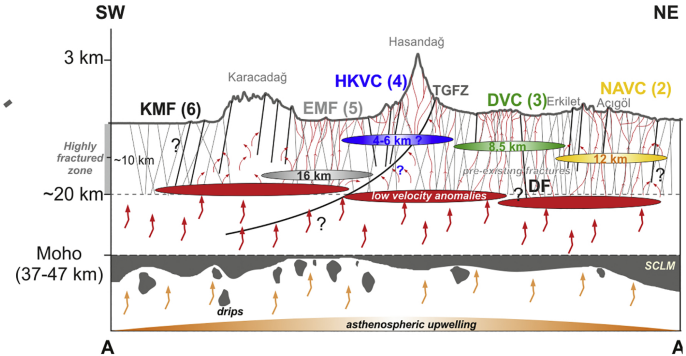
SW
NE
3 km
~20 km
Moho
(37-47 km)
Hasandağ
Karacadağ
HKVC (4)
TGFZ
DVC (3)
Erkilet
NAVC (2)
Acıgöl
KMF (6)
EMF (5)
Highly fractured zone
~10 km
4-6 km ?
8.5 km
12 km
16 km
pre-existing fractures
low velocity anomalies
DF
SCLM
drips
asthenospheric upwelling
A
A

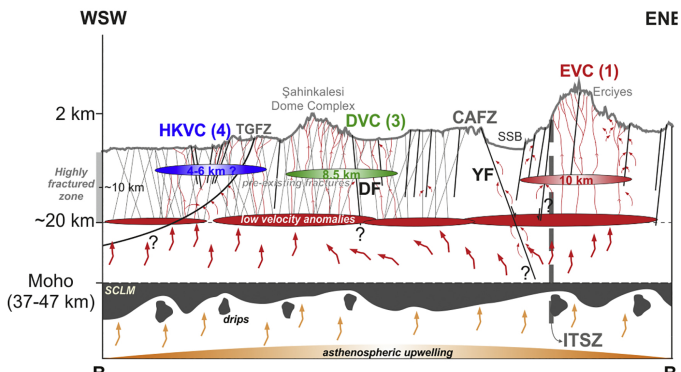
WSW
ENE
2 km
~20 km
Moho
(37-47 km)
EVC (1)
Erciyes
Şahinkalesi
Dome Complex
HKVC (4)
TGFZ
DVC (3)
CAFZ
SSB
YF
Highly fractured zone
~10 km
4-6 km ?
8.5 km
10 km
pre-existing fractures
DF
low velocity anomalies
SCLM
drips
ITSZ
asthenospheric upwelling
B
B

Figure 8